Supplementary Information for "Distributed multi-parameter quantum metrology on a superconducting quantum network"

CONTENTS

I. THEORETICAL ANALYSIS

A. General process of quantum metrology

The primary objective of quantum metrology is to precisely estimate unknown physical quantities by utilizing quantum resources, such as quantum entanglement. The general process of quantum metrology includes the following steps: state preparation, parameter encoding, measurement, and estimation. The probe state ρ_0 evolves under the given dynamics, which depend on the unknown parameters $\hat{x} = (x_1, \cdots, x_n)$, resulting in the encoded state $\rho(\hat{x})$. To extract information about the parameters $\hat{x}$, we perform a set of positive operator-valued measures (POVMs), represented as $\{\Pi_i\}$, on the state $\rho(\hat{x})$, obtaining a set of probability distributions $P_i(\hat{x})$, where $P_i(\hat{x})$ is the probability of obtaining the measurement result i. Finally, we construct the estimators $\hat{x}_{\text{est}} = (x_{1_{\text{est}}}, \cdots, x_{n_{\text{est}}})$ based on the probabilities of the measurement outcomes. For multi-parameter quantum estimating, the performance of locally unbiased estimators is quantified by the covariance matrix, where the jk-th element gives

$$[\text{Cov}(\hat{x})]_{jk} = E\left[(x_{j_{\text{est}}} - x_j)(x_{k_{\text{est}}} - x_k)\right]. \tag{S1}$$

The estimation precision for multiple parameters is quantified by the sum of variances, which corresponds to the sum of the diagonal terms of the covariance matrix. The covariance matrix is lower bounded by

$$\text{Cov}(\hat{x}) \geq \frac{1}{n} F_C^{-1} \tag{S2}$$

which is known as the Cramér-Rao bound. Here n is the number of measurement repetitions, and F_C is the Fisher information matrix (FIM) with jk-th element calculated as follows:

$$[F_C]_{x_j x_k} = \sum_i \frac{1}{P_i(\hat{x})} \left(\frac{\partial P_i(\hat{x})}{\partial x_j}\right) \left(\frac{\partial P_i(\hat{x})}{\partial x_k}\right) \tag{S3}$$

The Cramér-Rao bound is achievable for a large number of repetitions by using the maximum likelihood estimator (MLE). The quantum Cramér-Rao bound (QCRB) further constrains the covariance matrix:

$$\text{Cov}(\hat{x}) \geq \frac{1}{n} F_C^{-1} \geq \frac{1}{n} F_Q^{-1}. \tag{S4}$$

Here F_Q is the quantum Fisher information matrix (QFIM). For parameters encoded in pure states $|\psi_{\hat{x}}\rangle$, F_Q can be expressed as:

$$[F_Q]_{x_j x_k} = 4\,\text{Re}\left(\langle \partial_j \psi_{\hat{x}} | \partial_k \psi_{\hat{x}} \rangle - \langle \partial_j \psi_{\hat{x}} | \psi_{\hat{x}} \rangle \langle \psi_{\hat{x}} | \partial_k \psi_{\hat{x}} \rangle\right). \tag{S5}$$

More specifically, consider a pure probe state $|\psi_0\rangle$ undergoes a unitary process $U_{\hat{x}}$, the encoded state $|\psi_{\hat{x}}\rangle = U_{\hat{x}}|\psi_0\rangle$. Define the generator of $U_{\hat{x}}$ corresponding to unknown parameter x_j as

$$h_{x_j} = i U_{\hat{x}}^\dagger \left(\partial_{x_j} U_{\hat{x}}\right). \tag{S6}$$

Then, the quantum Fisher information matrix in Eq.(S5) can be expressed in terms of the generators,

$$[F_Q]_{x_j x_k} = 2\langle \psi_0 | \{h_{x_j}, h_{x_k}\} | \psi_0 \rangle - 4 \langle \psi_0 | h_{x_j} | \psi_0 \rangle \langle \psi_0 | h_{x_k} | \psi_0 \rangle. \tag{S7}$$

Here $\{\cdot,\cdot\}$ denotes the anti-commutator. According to QCRB, the precision of estimating multiple parameters is lower bound by $n\mathrm{Tr}(\mathrm{Cov}(\hat{x})) \geq \mathrm{Tr}(F_C^{-1}) \geq \mathrm{Tr}(F_Q^{-1})$. Hence, finding the maximal QFIM and the optimal measurement that saturates the QCRB leads to the ultimate precision of estimation. For multi-parameter quantum estimation, the necessary and sufficient condition for saturating the quantum Cramér-Rao bound in pure states is the weak commutativity condition, which is

$$\mathrm{Im}\left[\langle\partial_{x_j}\psi_{\hat{x}}|\partial_{x_k}\psi_{\hat{x}}\rangle\right] = 0, \forall x_j, x_k. \tag{S8}$$

To achieve the best precision for estimating unknown parameters $\hat{x}$, it is crucial to optimize every step of the process. This includes optimizing the initial state, adding additional controls, and performing the optimal measurement that saturates the quantum Cramér-Rao bound. In the control-enhanced sequential scheme, the total system evolution is described by $U_N = (U_c U_{\hat{x}})^N$, where $U_{\hat{x}}$ represents the system dynamics over encoding time T, and U_c denotes the control applied after each encoding time T. The optimal control strategy involves selecting $U_c = U_{\hat{x}}^\dagger$, as derived in [1]. With the implementation of N cycles of optimal control, the quantum Fisher information matrix becomes $N^2 F_Q$, reaching the Heisenberg limit. Here, F_Q denotes the QFIM for $N = 1$ without control, as adding only one control at the end of evolution cannot change the QFIM. To streamline the analysis, we examine the (maximal) QFIM for sensing strategies without control in the following sections. For cases with optimal control, the QFIM can be obtained by multiplying by N^2.

B. Sensing of a remote vector field

We consider the estimation of three components of a remote vector field, described in spherical coordinates (B, θ, ϕ) as $\vec{B} = (B\sin\theta\cos\phi, B\sin\theta\sin\phi, B\cos\theta)$, instead of in Cartesian coordinates $\vec{B} = (B_x, B_y, B_z)$. Estimating the vector field components $\vec{B} = (B_x, B_y, B_z)$ thus corresponds to simultaneously estimating the parameters $\hat{x} = (B, \theta, \phi)$. For each sensor qubit at time T, the evolution can be represented by $U_s = e^{-i\vec{B}\cdot\boldsymbol{\sigma}T} = e^{-iBT\boldsymbol{n}\cdot\boldsymbol{\sigma}}$ with $\boldsymbol{n} = (\sin\theta\cos\phi, \sin\theta\sin\phi, \cos\theta)$. The generator for $x_j \in \{B, \theta, \phi\}$ is given by

$$\begin{aligned} h_B &= c_B \boldsymbol{n}_B \cdot \boldsymbol{\sigma} \\ h_\theta &= c_\theta \boldsymbol{n}_\theta \cdot \boldsymbol{\sigma} \\ h_\phi &= c_\phi \boldsymbol{n}_\phi \cdot \boldsymbol{\sigma} \end{aligned} \tag{S9}$$

with

$$c_B = T, \quad c_\theta = \sin(BT), \quad c_\phi = \sin(BT)\sin\theta \tag{S10}$$

$$\begin{aligned} \boldsymbol{n}_B &= \boldsymbol{n} = (\sin\theta\cos\phi, \sin\theta\sin\phi, \cos\theta) \\ \boldsymbol{n}_\theta &= \cos(BT)\boldsymbol{n}_1 - \sin(BT)\boldsymbol{n}_2 \\ \boldsymbol{n}_\phi &= \sin(BT)\boldsymbol{n}_1 + \cos(BT)\boldsymbol{n}_2 \end{aligned} \tag{S11}$$

where $\boldsymbol{n}_1 = \partial_\theta \boldsymbol{n} = (\cos\theta\cos\phi, \cos\theta\sin\phi, -\sin\theta)$, $\boldsymbol{n}_2 = \boldsymbol{n} \times \boldsymbol{n}_1 = (-\sin\phi, \cos\phi, 0)$. It is easy to verify that $\boldsymbol{n}$, $\boldsymbol{n}_1$, $\boldsymbol{n}_2$ are orthogonal to each other. There exists a unitary transformation $U_r = e^{i\frac{BT}{2}\boldsymbol{n}\cdot\boldsymbol{\sigma}} e^{-i\frac{\phi}{2}\sigma_z} e^{-i\frac{\theta}{2}\sigma_y}$ such that

$$\boldsymbol{n}_B \cdot \boldsymbol{\sigma} = U_r \sigma_z U_r^\dagger, \quad \boldsymbol{n}_\theta \cdot \boldsymbol{\sigma} = U_r \sigma_x U_r^\dagger, \quad \boldsymbol{n}_\phi \cdot \boldsymbol{\sigma} = U_r \sigma_y U_r^\dagger, \tag{S12}$$

Assume the initial probe state is $|\psi_{SA}\rangle$, where the ancilla system is introduced. Then using Eq.(S7), we obtain the QFIM as

$$F_Q = 4 \begin{pmatrix} T^2 - (\mathrm{Tr}(\rho_S h_B))^2 & -\mathrm{Tr}(\rho_S h_B)\,\mathrm{Tr}(\rho_S h_\theta) & -\mathrm{Tr}(\rho_S h_B)\,\mathrm{Tr}(\rho_S h_\phi) \\ -\mathrm{Tr}(\rho_S h_B)\,\mathrm{Tr}(\rho_S h_\theta) & \sin^2(BT) - (\mathrm{Tr}(\rho_S h_\theta))^2 & -\mathrm{Tr}(\rho_S h_\theta)\,\mathrm{Tr}(\rho_S h_\phi) \\ -\mathrm{Tr}(\rho_S h_B)\,\mathrm{Tr}(\rho_S h_\phi) & -\mathrm{Tr}(\rho_S h_\theta)\,\mathrm{Tr}(\rho_S h_\phi) & \sin^2(BT)\sin^2\theta - (\mathrm{Tr}(\rho_S h_\theta))^2 \end{pmatrix} \tag{S13}$$

where $\rho_S = \mathrm{Tr}_A(|\psi_{SA}\rangle\langle\psi_{SA}|)$ denotes the reduced state by tracing out the ancilla system. The maximal QFIM, denoted as $F_Q^{\max}$, is

$$F_Q^{\max} = 4 \begin{pmatrix} T^2 & 0 & 0 \\ 0 & \sin^2(BT) & 0 \\ 0 & 0 & \sin^2(BT)\sin^2\theta \end{pmatrix}. \tag{S14}$$

F_Q^{max} represents the upper limit of the QFIM under optimal conditions. This is because $F_Q^{max} - F_Q$ is always a positive semi-definite matrix, a property that signifies no other state can yield a higher QFIM value. The maximal QFIM is achieved when choosing $\rho_S = \frac{1}{2}I$, indicating that the optimal initial state for maximizing the QFIM is a maximally entangled state, denoted as $|\psi_{SA}\rangle = \frac{1}{\sqrt{2}}(|00\rangle + |11\rangle)$. The projective measurement in the Bell basis is the optimal measurement that saturates the quantum Cramér-Rao bound, which is given as

$$M_{00} = \left|\Phi^+\right\rangle\left\langle\Phi^+\right|, \quad M_{01} = \left|\Phi^-\right\rangle\left\langle\Phi^-\right|, \quad M_{10} = \left|\Psi^+\right\rangle\left\langle\Psi^+\right|, \quad M_{11} = \left|\Psi^-\right\rangle\left\langle\Psi^-\right|, \tag{S15}$$

where the Bell states are given by:

$$\begin{aligned} \left|\Phi^+\right\rangle &= \frac{1}{\sqrt{2}}(|00\rangle + |11\rangle), \quad \left|\Phi^-\right\rangle = \frac{1}{\sqrt{2}}(|00\rangle - |11\rangle), \\ \left|\Psi^+\right\rangle &= \frac{1}{\sqrt{2}}(|01\rangle + |10\rangle), \quad \left|\Psi^-\right\rangle = \frac{1}{\sqrt{2}}(|01\rangle - |10\rangle). \end{aligned} \tag{S16}$$

The probability of the measurement results in the Bell basis

$$\begin{aligned} P_{00} &= \mathrm{Tr}(\rho(B,\theta,\phi)M_{00}) = \cos^2(BT) \\ P_{01} &= \mathrm{Tr}(\rho(B,\theta,\phi)M_{01}) = \sin^2(BT)\cos^2\theta \\ P_{10} &= \mathrm{Tr}(\rho(B,\theta,\phi)M_{10}) = \sin^2(BT)\sin^2\theta\cos^2\phi \\ P_{11} &= \mathrm{Tr}(\rho(B,\theta,\phi)M_{11}) = \sin^2(BT)\sin^2\theta\sin^2\phi \end{aligned} \tag{S17}$$

where $\rho(B,\theta,\phi) = (U_s \otimes I)|\psi_{SA}\rangle\langle\psi_{SA}|(U_s^\dagger \otimes I)$ is density matrix for the evolved state. Based on the probability distribution, by using Eq.(S3), it is straightforward to verify the classical Fisher information matrix equals the quantum Fisher information matrix, thereby saturating the quantum Cramér-Rao bound. The estimated precision limits for vector components are given by:

$$\delta B_{\mathrm{est}}^2 \geq \frac{1}{4T^2}, \quad \delta\theta_{\mathrm{est}}^2 \geq \frac{1}{4\sin^2(BT)}, \quad \delta\phi_{\mathrm{est}}^2 \geq \frac{1}{4\sin^2(BT)\sin^2\theta} \tag{S18}$$

Following the error propagation formula, we calculate:

$$\begin{aligned}
\delta B_{x_{\text{est}}} &= \sin\theta\cos\phi\delta B_{\text{est}} + B\cos\theta\cos\phi\delta\theta_{\text{est}} - B\sin\theta\sin\phi\delta\phi_{\text{est}} \\
\delta B_{y_{\text{est}}} &= \sin\theta\sin\phi\delta B_{\text{est}} + B\cos\theta\sin\phi\delta\theta_{\text{est}} + B\sin\theta\cos\phi\delta\phi_{\text{est}} \\
\delta B_{z_{\text{est}}} &= \cos\theta\delta B_{\text{est}} - B\sin\theta\delta\theta_{\text{est}}
\end{aligned} \tag{S19}$$

The summation of squared deviations gives the precision limits for estimating three components of a vector field:

$$\begin{aligned}
\delta B_{x_{\text{est}}}^2 + \delta B_{y_{\text{est}}}^2 + \delta B_{z_{\text{est}}}^2 &= \delta B_{\text{est}}^2 + B^2\delta\theta_{\text{est}}^2 + B^2\sin^2\theta\delta\phi_{\text{est}}^2 \\
&\geq \frac{1}{4T^2} + \frac{B^2}{2\sin^2(BT)}.
\end{aligned} \tag{S20}$$

C. Sensing of the gradients between vector fields

In this section, we consider the estimation of the gradients between two remote vector fields, expressed as $\nabla\vec{B} = \vec{B}_1 - \vec{B}_2 = (\nabla B_x, \nabla B_y, \nabla B_z)$. For each sensor qubit, the Hamiltonian H_j is given by $H_j = \vec{B}_j\cdot\boldsymbol{\sigma} = B_{jx}\sigma_x + B_{jy}\sigma_y + B_{jz}\sigma_z$, where $\vec{B}_j = (B_{jx}, B_{jy}, B_{jz})$ represents the vector field components and $\boldsymbol{\sigma} = (\sigma_x, \sigma_y, \sigma_z)$ denotes the spin vector. Alternatively, in spherical coordinates, the Hamiltonian is represented as $H_j = B_j\boldsymbol{n}_j\cdot\boldsymbol{\sigma}$, where $\boldsymbol{n}_j = (\sin\theta_j\cos\phi_j, \sin\theta_j\sin\phi_j, \cos\theta_j)$ and $B_j = \sqrt{B_{jx}^2 + B_{jy}^2 + B_{jz}^2}$ represents the magnitude of the vector field. The evolution at time T can be represented by $U_{sj} = e^{-i\vec{B}_j\cdot\boldsymbol{\sigma}T} = e^{-iB_j\boldsymbol{n}_j\cdot\boldsymbol{\sigma}T}$ for $j = 1, 2$.

We evaluate the precision of two strategies for estimating vector field gradients. The first strategy employs non-local entanglement, directly estimating the vector field gradient by leveraging entanglement across the sensor network. The second uses local entanglement, measuring each vector field independently at the two locations and then calculating the gradient. Our comparison highlights the precision benefits of distributed quantum sensing, with non-local entanglement offering distinct advantages for accurate gradient estimation.

1. Non-local entanglement

Utilizing non-local entanglement enables the direct and simultaneous estimation of spatial gradients, potentially giving higher precision. In this approach, we introduce a 4-qubit non-local entangled state as the probe state, $|\Psi_0\rangle = \frac{1}{\sqrt{2}}(|0011\rangle - |1100\rangle)$, to directly estimate gradients along three directions. The first two qubits and the last two qubits are sent to two separate sensor modules (module $\mathcal{B}$ and $\mathcal{C}$ in the main text), respectively. The total evolution of the dynamics is expressed as $U_{\text{S}} = U_{s1}\otimes U_{s1}\otimes U_{s2}\otimes U_{s2}$, which gives the evolved state as $U_{\text{S}}|\Psi_0\rangle$, containing the information of the spatial gradients. Denote the sum of two vector fields as $\sum\vec{B} = \vec{B}_1 + \vec{B}_2 = (\sum B_x, \sum B_y, \sum B_z)$. The components of the vector field can then be rewritten as

$$B_{1p} = \frac{\sum B_p + \nabla B_p}{2}, \quad B_{2p} = \frac{\sum B_p - \nabla B_p}{2}, \quad \text{for } p \in \{x, y, z\}. \tag{S21}$$

To effectively estimate the gradients, denoted as $\nabla\vec{B}$, it is also necessary to acquire information about the sum of the vector fields, denoted here as $\sum\vec{B}$. This information is crucial for adaptively implementing control strategies. Such control strategies essentially reduce the problem of estimating general gradients $\nabla\vec{B}$ to estimating $\nabla\vec{B}=(0,0,0)$, indicating $\vec{B}_1=\vec{B}_2=\vec{B}$. This can be realized by adding compensation to the vector fields if the gradients are non-zero. Therefore, we benchmark the performance of our estimation protocol at zero-gradient, and the comparison of different strategies will also be made under this assumption.

Under the dynamics governed by U_{S}, the quantum Fisher information matrix for simultaneously estimating $\hat{x}=(\nabla\vec{B},\sum\vec{B})$ is given by

$$F_Q=\begin{pmatrix}F_- & \mathbf{0}\\ \mathbf{0} & F_+\end{pmatrix}, \tag{S22}$$

where this matrix is block-diagonal,with F_- and F_+ representing the QFIM for estimating $\nabla\vec{B}=(\nabla B_x,\nabla B_y,\nabla B_z)$ and $\sum\vec{B}=(\sum B_x,\sum B_y,\sum B_z)$, respectively, which are given by

$$F_-=\begin{pmatrix}[F_Q]_{\nabla B_x\nabla B_x} & [F_Q]_{\nabla B_x\nabla B_y} & [F_Q]_{\nabla B_x\nabla B_z}\\ [F_Q]_{\nabla B_x\nabla B_y} & [F_Q]_{\nabla B_y\nabla B_y} & [F_Q]_{\nabla B_y\nabla B_z}\\ [F_Q]_{\nabla B_x\nabla B_z} & [F_Q]_{\nabla B_y\nabla B_z} & [F_Q]_{\nabla B_z\nabla B_z}\end{pmatrix}, \tag{S23}$$

with

$$\begin{aligned}
[F_Q]_{\nabla B_x\nabla B_x}=&\frac{4}{B^4}\left(B_x^2T^2(B^2+3B_z^2)+\sin^2(BT)(B_y^2+B_z^2+6B_xB_yB_zT+3B_y^2\sin^2(BT))\right)\\
&+\frac{3B_xB_z\sin(2BT)}{B^6}\left(-4BB_y\sin^2(BT)+B_xB_z(-4BT+\sin(2BT)\right),\\
[F_Q]_{\nabla B_y\nabla B_y}=&\frac{4}{B^4}\left(B_y^2T^2(B^2+3B_z^2)+\sin^2(BT)(B_x^2+B_z^2-6B_xB_yB_zT+3B_x^2\sin^2(BT))\right)\\
&+\frac{3B_yB_z\sin(2BT)}{B^6}\left(4BB_x\sin^2(BT)+B_yB_z(-4BT+\sin(2BT)\right)\\
[F_Q]_{\nabla B_z\nabla B_z}=&\frac{4}{B^4}\left(B_z^2T^2(B^2+3B_z^2)+\sin^2(BT)(B_x^2+B_y^2)\right)\\
&+\frac{3\sin(2BT)}{B^6}\left(4B(B_x^2+B_y^2)B_z^2T+(B_x^2+B_y^2)^2\sin(2BT)\right),\\
[F_Q]_{\nabla B_x\nabla B_y}=&\frac{4}{B^4}\left(B_xB_yT^2(B^2+3B_z^2)-\sin^2(BT)(4B_xB_y+3B_zT(B_x^2-B_y^2))\right)\\
&+\frac{3\sin(2BT)}{B^6}\left(2BB_z\sin^2(BT)(B_x^2-B_y^2)+B_xB_y(-4BB_z^2T+(B^2+B_z^2)\sin(2BT))\right),\\
[F_Q]_{\nabla B_x\nabla B_z}=&\frac{4B_z}{B^4}\left(B_xT^2(B^2+3B_z^2)-\sin^2(BT)(B_x-3B_yB_zT)\right)\\
&+\frac{3\sin(2BT)}{B^6}\left(2BB_y\sin^2(BT)(B_x^2+B_y^2)+B_xB_z(2BT(B^2-2B_z^2)-(B^2-B_z^2)\sin(2BT))\right),\\
[F_Q]_{\nabla B_y\nabla B_z}=&\frac{4B_z}{B^4}\left(B_yT^2(B^2+3B_z^2)-\sin^2(BT)(B_y+3B_xB_zT)\right)\\
&-\frac{3\sin(2BT)}{B^6}\left(2BB_x\sin^2(BT)(B_x^2+B_y^2)-B_yB_z(2BT(B^2-2B_z^2)-(B^2-B_z^2)\sin(2BT))\right),
\end{aligned} \tag{S24}$$

and

$$F_+=\begin{pmatrix}[F_Q]_{\sum B_x\sum B_x} & [F_Q]_{\sum B_x\sum B_y} & [F_Q]_{\sum B_x\sum B_z}\\ [F_Q]_{\sum B_x\sum B_y} & [F_Q]_{\sum B_y\sum B_y} & [F_Q]_{\sum B_y\sum B_z}\\ [F_Q]_{\sum B_x\sum B_z} & [F_Q]_{\sum B_y\sum B_z} & [F_Q]_{\sum B_z\sum B_z}\end{pmatrix}, \tag{S25}$$

with

$$
\begin{aligned}
[F_Q]_{\sum B_x \sum B_x} =& \frac{4}{B^4}\left(B_x^2T^2(B_x^2+B_y^2)+B_z\sin^2(BT)(B_z-2B_xB_yT)\right)\\
&+\frac{\sin(2BT)}{B^6}\left(4BB_x^2B_z^2T+4BB_xB_yB_z\sin^2(BT)+(B^2B_y^2-B_x^2B_z^2)\sin(2BT)\right),\\
[F_Q]_{\sum B_y \sum B_y} =& \frac{4}{B^4}\left(B_y^2T^2(B_x^2+B_y^2)+B_z\sin^2(BT)(B_z+2B_xB_yT)\right)\\
&+\frac{\sin(2BT)}{B^6}\left(4BB_y^2B_z^2T-4BB_xB_yB_z\sin^2(BT)+(B^2B_x^2-B_y^2B_z^2)\sin(2BT)\right),\\
[F_Q]_{\sum B_z \sum B_z} =& \frac{4}{B^4}(B_x^2+B_y^2)(B_z^2T^2+\sin^2(BT))\\
&+\frac{\sin(2BT)}{B^6}(B_x^2+B_y^2)\left(4BB_z^2T+(B_x^2+B_y^2)\sin(2BT)\right)\\
[F_Q]_{\sum B_x \sum B_y} =& \frac{4T}{B^4}\left(B_xB_yT(B_x^2+B_y^2)+B_z\sin^2(BT)(B_x^2-B_y^2)\right)\\
&+\frac{\sin(2BT)}{B^6}\left(4BB_xB_yB_z^2T-2BB_z\sin^2(BT)(B_x^2-B_y^2)-B_xB_y\sin(2BT)(B^2+B_z^2)\right),\\
[F_Q]_{\sum B_x \sum B_z} =& \frac{4B_z}{B^4}\left(B_xT^2(B_x^2+B_y^2)-\sin^2(BT)(B_x+B_yB_zT)\right)\\
&-\frac{\sin(2BT)}{B^6}\left(2BB_xB_zT(B^2-2B_z^2)+(B_x^2+B_y^2)\left(2BB_y\sin^2(BT)-B_xB_z\sin(2BT)\right)\right),\\
[F_Q]_{\sum B_y \sum B_z} =& \frac{4B_z}{B^4}\left(B_yT^2(B_x^2+B_y^2)-\sin^2(BT)(B_y-B_xB_zT)\right)\\
&-\frac{\sin(2BT)}{B^6}\left(2BB_yB_zT(B^2-2B_z^2)-(B_x^2+B_y^2)\left(2BB_x\sin^2(BT)+B_yB_z\sin(2BT)\right)\right).
\end{aligned}
\tag{S26}
$$

Since the QFIM takes a block diagonal form, the estimation of the sum vector $\sum\vec{B}$ does not influence the precision of estimating the gradients $\nabla\vec{B}$, which can be expressed as:

$$
(\delta\nabla B_{x_{\text{est}}})^2+(\delta\nabla B_{y_{\text{est}}})^2+(\delta\nabla B_{z_{\text{est}}})^2\geq \text{Tr}\left(F_-^{-1}\right)=\frac{4B^2-3B_z^2}{16B^2T^2}+\frac{5B^2+3B_z^2}{16\sin^2(BT)},
\tag{S27}
$$

where $B=\sqrt{B_x^2+B_y^2+B_z^2}$. We can verify that the weak commutativity condition in Eq.(S8) is satisfied, indicating the existence of a set of POVM that saturates the QCRB, achieving this precision.

For easier experimental realization, we consider performing local separable measurements on each sensor module ($\mathcal{B}$ and $\mathcal{C}$). Specifically, one can choose the projective measurement in Bell basis on each sensor module as follows:

$$
\Pi_{\mathcal{X}_{00}}=\left|\Phi^+\right\rangle\left\langle\Phi^+\right|,\quad \Pi_{\mathcal{X}_{01}}=\left|\Phi^-\right\rangle\left\langle\Phi^-\right|,\quad \Pi_{\mathcal{X}_{10}}=\left|\Psi^+\right\rangle\left\langle\Psi^+\right|,\quad \Pi_{\mathcal{X}_{11}}=\left|\Psi^-\right\rangle\left\langle\Psi^-\right|,
\tag{S28}
$$

where $\mathcal{X}\in\{\mathcal{B},\mathcal{C}\}$ denoted the sensor module and the Bell states are given in Eq.(S16). This construction forms 16 measurement basis $\Pi_k=\Pi_{\mathcal{B}_i}\otimes\Pi_{\mathcal{C}_j}$, $\forall i,j\in\{00,01,10,11\}$, satisfying $\sum_{k\in\{0000,\cdots,1111\}}\Pi_k=I$. The probability distribution of the measurement outcome under $\{\Pi_k\}$ gives $P_k=\langle\Psi_{\hat{x}}|\Pi_k|\Psi_{\hat{x}}\rangle$ for $k\in\{0000,0001,\cdots,1111\}$, where $|\Psi_{\hat{x}}\rangle=U_{\text{S}}|\Psi_0\rangle$ is the evolved state. For certain measurement outcomes, such as $\{0011,0111,1011,1100,1101,1110,1111\}$, $P_k=0$ regardless of the real values of $\nabla B_x,\nabla B_y,\nabla B_z$, indicating no information about the parameters can be obtained from these outcomes. In contrast, for $k\in\{0000,0101,1010\}$, $P_k=0$ specifically at the zero-gradient, where $\nabla\vec{B}=(0,0,0)$. Even in this scenario, where the probability distribution equals zero at specific values, the probability distribution still contains implicit parameter information.

The classical Fisher information matrix (CFIM) depends on the derivative of P_k with respect to $x_i, x_j \in \{\nabla B_x, \nabla B_y, \nabla B_z, \sum B_x, \sum B_y, \sum B_z\}$, calculated as follows:

$$\begin{aligned}
[F_C]_{x_i x_j} &= \sum_k \frac{1}{P_k}\left(\frac{\partial P_k}{\partial x_i}\right)\left(\frac{\partial P_k}{\partial x_j}\right) \\
&= \sum_k \frac{\left(\partial x_i \langle\Psi_{\hat{x}}|\Pi_k|\Psi_{\hat{x}}\rangle\right)\left(\partial x_j \langle\Psi_{\hat{x}}|\Pi_k|\Psi_{\hat{x}}\rangle\right)}{\langle\Psi_{\hat{x}}|\Pi_k|\Psi_{\hat{x}}\rangle} \\
&= \sum_k \frac{4\mathrm{Re}\left(\langle\partial x_i \Psi_{\hat{x}}|\Pi_k|\Psi_{\hat{x}}\rangle\right)\mathrm{Re}\left(\langle\partial x_j \Psi_{\hat{x}}|\Pi_k|\Psi_{\hat{x}}\rangle\right)}{\langle\Psi_{\hat{x}}|\Pi_k|\Psi_{\hat{x}}\rangle}
\end{aligned} \tag{S29}$$

where $k \in \{0000, 0001, 0010, 0100, 0101, 0110, 1000, 1001, 1010\}$. Specifically, at $\nabla B_x = 0, \nabla B_y = 0$ and $\nabla B_z = 0$, $P_k = \langle\Psi_{\hat{x}}|\Pi_k|\Psi_{\hat{x}}\rangle = 0$, $\mathrm{Re}\left(\langle\partial x_i \Psi_{\hat{x}}|\Pi_k|\Psi_{\hat{x}}\rangle\right) = 0$ for $k \in \{0000, 0101, 1010\}$. In these cases, the term is of the form $\frac{0}{0}$ which needs to be calculated via limit. For these term, $[F_C]_{x_i x_j}$ can be calculated when the parameters $\nabla B_x, \nabla B_y$ and ∇B_z are displaced by an arbitrary small disturbance, replacing $|\Psi_{\hat{x}}\rangle$ with $|\Psi_{\hat{x}}\rangle + \sum_{l=1}^{6} \delta x_l \, |\partial_{x_l} \Psi_{\hat{x}}\rangle$, where $x_1 = \nabla B_x, x_2 = \nabla B_y, x_3 = \nabla B_z, x_4 = \sum B_x, x_5 = \sum B_y, x_6 = \sum B_z$. Thus, it can be verified that for $\forall x_i, x_j \in \{\nabla B_x, \nabla B_y, \nabla B_z, \sum B_x, \sum B_y, \sum B_z\}$,

$$\begin{aligned}
[F_C]_{x_i x_j} &= \sum_{k_1} \frac{\sum_{l_1=1}^{6}\sum_{l_2=1}^{6} 4\delta x_{l_1}\delta x_{l_2}\mathrm{Re}\left(\langle\partial x_i \Psi_{\hat{x}}|\Pi_{k_1}|\partial x_{l_1}\Psi_{\hat{x}}\rangle\right)\mathrm{Re}\left(\langle\partial x_{l_2}\Psi_{\hat{x}}|\Pi_{k_1}|\partial x_j \Psi_{\hat{x}}\rangle\right)}{\sum_{l_1=1}^{6}\sum_{l_2=1}^{6}\delta x_{l_1}\delta x_{l_2}\langle\partial x_{l_1}\Psi_{\hat{x}}|\Pi_{k_1}|\partial x_{l_2}\Psi_{\hat{x}}\rangle} \\
&\quad + \sum_{k_2} \frac{4\mathrm{Re}\left(\langle\partial x_i \Psi_{\hat{x}}|\Pi_{k_2}|\Psi_{\hat{x}}\rangle\right)\mathrm{Re}\left(\langle\partial x_j \Psi_{\hat{x}}|\Pi_{k_2}|\Psi_{\hat{x}}\rangle\right)}{\langle\Psi_{\hat{x}}|\Pi_{k_2}|\Psi_{\hat{x}}\rangle} \\
&= [F_Q]_{x_i x_j}
\end{aligned} \tag{S30}$$

where $k_1 \in \{0000, 0101, 1010\}$ and $k_2 \in \{0001, 0010, 0100, 0110, 1000, 1001\}$. This demonstrates that the QCRB can be saturated by performing local projective measurement in the Bell basis on each sensor module, indicating the precision in Eq.(S27) is achievable.

Here, we also provide the precision achievable in estimating two components of gradients, specifically ∇B_x and ∇B_y, using the same non-local entangled probe state $|\Psi_0\rangle$. The quantum Fisher information matrix for simultaneously estimating $\nabla B_x, \nabla B_y, \sum B_x, \sum B_y$ also takes the block diagonal form in Eq.(S22), with F_- and F_+ given by

$$F_- = \begin{pmatrix} [F_Q]_{\nabla B_x \nabla B_x} & [F_Q]_{\nabla B_x \nabla B_y} \\ [F_Q]_{\nabla B_x \nabla B_y} & [F_Q]_{\nabla B_y \nabla B_y} \end{pmatrix}, \quad F_+ = \begin{pmatrix} [F_Q]_{\sum B_x \sum B_x} & [F_Q]_{\sum B_x \sum B_y} \\ [F_Q]_{\sum B_x \sum B_y} & [F_Q]_{\sum B_y \sum B_y} \end{pmatrix}, \tag{S31}$$

where

$$
\begin{aligned}
[F_Q]_{\nabla B_x \nabla B_x} =& \frac{4B_x^2T^2}{B^2} + \frac{B_y^2\left(16\sin^2(BT) - 3\sin^2(2BT)\right)}{B^4}, \\
[F_Q]_{\nabla B_y \nabla B_y} =& \frac{4B_y^2T^2}{B^2} + \frac{B_x^2\left(16\sin^2(BT) - 3\sin^2(2BT)\right)}{B^4}, \\
[F_Q]_{\nabla B_x \nabla B_y} =& \frac{4B_xB_yT^2}{B^2} - \frac{B_xB_y\left(16\sin^2(BT) - 3\sin^2(2BT)\right)}{B^4}, \\
[F_Q]_{\sum B_x \sum B_x} =& \frac{4B_x^2T^2}{B^2} + \frac{B_y^2\sin^2(2BT)}{B^4}, \\
[F_Q]_{\sum B_y \sum B_y} =& \frac{4B_y^2T^2}{B^2} + \frac{B_x^2\sin^2(2BT)}{B^4}, \\
[F_Q]_{\sum B_x \sum B_y} =& \frac{4B_xB_yT^2}{B^2} - \frac{B_xB_y\sin^2(2BT)}{B^4},
\end{aligned}
\tag{S32}
$$

with $B = \sqrt{B_x^2 + B_y^2}$. The quantum Cramér-Rao bound can be saturated by performing projective measurement in Bell basis on each sensor module, where the proof of optimal measurement is similar to the three-component case and is omitted for brevity. Hence, the precision of estimating gradients is

$$
\delta\nabla B_{x_{\text{est}}}^2 + \delta\nabla B_{y_{\text{est}}}^2 \geq \frac{1}{4T^2} + \frac{B^2}{4\left(1 + 3\sin^2(BT)\right)\sin^2(BT)}. \tag{S33}
$$

2. *Local entanglement*

To estimate the gradients between remote vector fields, a straightforward approach is to first estimate each vector field independently, then calculate the gradient. In this method, we use a 2-qubit locally entangled state to estimate the three components of each vector field. The unitary dynamics governing this system is represented by $U_s \otimes U_s$, where $U_s = e^{-iBT\boldsymbol{n}\cdot\boldsymbol{\sigma}}$. The analysis of precision limits follows [2]. The generator corresponding to the parameter $x_j \in \{B, \theta, \phi\}$ is

$$
\begin{aligned}
G_{x_j} &= i\left(U_s^\dagger \otimes U_s^\dagger\right)\left(\partial_{x_j}U_s \otimes U_s + U_s \otimes \partial_{x_j}U_s\right) \\
&= h_{x_j} \otimes I_2 + I_2 \otimes h_{x_j}
\end{aligned}
\tag{S34}
$$

where h_{x_j} is given in Eq.(S9). By Eq.(S7), the diagonal elements of QFIM can be expressed as the variance of the generators G_{x_j},

$$
[F_Q]_{x_jx_j} = 4\langle\Delta^2 G_{x_j}\rangle = 4\left(\langle G_{x_j}^2\rangle - \langle G_{x_j}\rangle^2\right), \tag{S35}
$$

where the term $\langle G_{x_j}^2\rangle$ and $\langle G_{x_j}\rangle^2$ can be expanded as

$$
\begin{aligned}
&\langle G_{x_j}^2\rangle = \langle h_{x_j}^2 \otimes I\rangle + \langle I \otimes h_{x_j}^2\rangle + 2\langle h_{x_j} \otimes h_{x_j}\rangle = 2c_{x_j}^2 + 2c_{x_j}^2 r_{x_jx_j}, \\
&\langle G_{x_j}\rangle^2 = c_{x_j}^2(r_{x_j}^{(1)} + r_{x_j}^{(2)})^2.
\end{aligned}
\tag{S36}
$$

Here $r_{x_jx_j} = \text{Tr}[\rho_{SS}(\boldsymbol{n}_{x_j}\cdot\boldsymbol{\sigma}) \otimes (\boldsymbol{n}_{x_j}\cdot\boldsymbol{\sigma})]$, where ρ_{SS} is the density matrix for the probe state and $\boldsymbol{n}_{x_j}$ are detailed in Eq.(S11). $r_{x_j}^{(1)} = \text{Tr}[\rho_S^{(1)}\boldsymbol{n}_{x_j}\cdot\boldsymbol{\sigma}]$ and $r_{x_j}^{(2)} = \text{Tr}[\rho_S^{(2)}\boldsymbol{n}_{x_j}\cdot\boldsymbol{\sigma}]$, where $\rho_S^{(1)}$ and $\rho_S^{(2)}$ are the reduced matrices of ρ_{SS} the first and second qubits.

For each parameter $x_j \in \{B, \theta, \phi\}$, we have $\delta x_{j_{\text{est}}}^2 \geq \frac{1}{4\langle \Delta^2 G_{x_j} \rangle}$, thus

$$
\begin{aligned}
& w_B \delta B_{\text{est}}^2 + w_\theta \delta\theta_{\text{est}}^2 + w_\phi \delta\phi_{\text{est}}^2 \\
\geq & \frac{1}{4}\left(\frac{w_B}{\langle \Delta^2 G_B \rangle} + \frac{w_\theta}{\langle \Delta^2 G_\theta \rangle} + \frac{w_\phi}{\langle \Delta^2 G_\phi \rangle} \right) \\
= & \frac{1}{4}\left(\frac{w_B/T^2}{2 + 2r_{BB} - \left(r_B^{(1)} + r_B^{(2)}\right)^2} + \frac{w_\theta/\sin^2(BT)}{2 + 2r_{\theta\theta} - \left(r_\theta^{(1)} + r_\theta^{(2)}\right)^2} + \frac{w_\phi/\sin^2(BT)\sin\theta^2}{2 + 2r_{\phi\phi} - \left(r_\phi^{(1)} + r_\phi^{(2)}\right)^2} \right) \\
\geq & \frac{1}{4}\left(\frac{w_B/T^2}{2 + 2r_{BB}} + \frac{w_\theta/\sin^2(BT)}{2 + 2r_{\theta\theta}} + \frac{w_\phi/\sin^2(BT)\sin\theta^2}{2 + 2r_{\phi\phi}} \right) \\
\overset{a)}{\geq} & \frac{\left(\frac{\sqrt{w_B}}{T} + \frac{\sqrt{w_\theta}}{|\sin(BT)|} + \frac{\sqrt{w_\phi}}{|\sin(BT)\sin\theta|} \right)^2}{4(2 + 2r_{BB} + 2 + 2r_{\theta\theta} + 2 + 2r_{\phi\phi})} \\
\overset{b)}{\geq} & \frac{\left(\frac{\sqrt{w_B}}{T} + \frac{\sqrt{w_\theta}}{|\sin(BT)|} + \frac{\sqrt{w_\phi}}{|\sin(BT)\sin\theta|} \right)^2}{32}
\end{aligned}
\tag{S37}
$$

where the inequality $a)$ follows from the Cauchy-Schwarz inequality, and the inequality $b)$ uses the fact that $r_{BB} + r_{\theta\theta} + r_{\phi\phi} \leq 1$. To prove this fact, we write a general two-qubit state ρ as

$$
\rho = \frac{1}{4}[I_4 + \sum_l r_l^{(1)} \sigma_l \otimes I + \sum_p r_p^{(2)} I \otimes \sigma_p + \sum_{l,p} r_{l,p} \sigma_l \otimes \sigma_p] \tag{S38}
$$

where $l, p \in \{x, y, z\}$. Let $\rho_{SS} = (U_r \otimes U_r)\rho(U_r^\dagger \otimes U_r^\dagger)$, by using the properties in Eq.(S12), we have $r_{xx} = \text{Tr}[\rho(\sigma_x \otimes \sigma_x)] = \text{Tr}\left[\rho_{SS}\left(\boldsymbol{n}_\theta \cdot \boldsymbol{\sigma} \otimes \boldsymbol{n}_\theta \cdot \boldsymbol{\sigma}\right)\right] = r_{\theta\theta}$, $r_{yy} = \text{Tr}[\rho(\sigma_y \otimes \sigma_y)] = \text{Tr}\left[\rho_{SS}\left(\boldsymbol{n}_\phi \cdot \boldsymbol{\sigma} \otimes \boldsymbol{n}_\phi \cdot \boldsymbol{\sigma}\right)\right] = r_{\phi\phi}$ and $r_{zz} = \text{Tr}[\rho(\sigma_z \otimes \sigma_z)] = \text{Tr}\left[\rho_{SS}\left(\boldsymbol{n}_B \cdot \boldsymbol{\sigma} \otimes \boldsymbol{n}_B \cdot \boldsymbol{\sigma}\right)\right] = r_{BB}$. Since the density matrix ρ is always positive semi-definite, let $r_l^{(1)} = 0$, $r_p^{(2)} = 0$ for $\forall l, p \in \{x, y, z\}$, and $r_{l,p} = 0$ for $l \neq q$, we have all the eigenvalues of ρ are non-negative, which gives the following constraints:

$$
\begin{aligned}
r_{xx} + r_{yy} + r_{zz} &\leq 1 \\
r_{zz} - r_{xx} - r_{yy} &\leq 1 \\
r_{yy} - r_{xx} - r_{zz} &\leq 1 \\
r_{xx} - r_{yy} - r_{zz} &\leq 1
\end{aligned}
\tag{S39}
$$

The first inequality is equivalent to $r_{BB} + r_{\theta\theta} + r_{\phi\phi} \leq 1$. Hence, the lower bound on the figure of merit can be obtained as:

$$
w_B \delta B_{\text{est}}^2 + w_\theta \delta\theta_{\text{est}}^2 + w_\phi \delta\phi_{\text{est}}^2 \geq \frac{\left(\frac{\sqrt{w_B}}{T} + \frac{\sqrt{w_\theta}}{|\sin(BT)|} + \frac{\sqrt{w_\phi}}{|\sin(BT)\sin\theta|} \right)^2}{32} \tag{S40}
$$

which can be saturated when

$$
\begin{aligned}
r_{BB}^{opt} &= \frac{3\frac{\sqrt{w_B}}{T} - \frac{\sqrt{w_\theta}}{|\sin(BT)|} - \frac{\sqrt{w_\phi}}{|\sin(BT)\sin\theta|}}{\frac{\sqrt{w_B}}{T} + \frac{\sqrt{w_\theta}}{|\sin(BT)|} + \frac{\sqrt{w_\phi}}{|\sin(BT)\sin\theta|}} \\
r_{\theta\theta}^{opt} &= \frac{3\frac{\sqrt{w_\theta}}{|\sin(BT)|} - \frac{\sqrt{w_B}}{T} - \frac{\sqrt{w_\phi}}{|\sin(BT)\sin\theta|}}{\frac{\sqrt{w_B}}{T} + \frac{\sqrt{w_\theta}}{|\sin(BT)|} + \frac{\sqrt{w_\phi}}{|\sin(BT)\sin\theta|}} \\
r_{\phi\phi}^{opt} &= \frac{3\frac{\sqrt{w_\phi}}{|\sin(BT)\sin\theta|} - \frac{\sqrt{w_B}}{T} - \frac{\sqrt{w_\theta}}{|\sin(BT)|}}{\frac{\sqrt{w_B}}{T} + \frac{\sqrt{w_\theta}}{|\sin(BT)|} + \frac{\sqrt{w_\phi}}{|\sin(BT)\sin\theta|}}
\end{aligned}
\tag{S41}
$$

and $r_B^{(1)} + r_B^{(2)} = r_\theta^{(1)} + r_\theta^{(2)} = r_\phi^{(1)} + r_\phi^{(2)} = 0$. The lower bound can be saturated when the reduced two-qubit state takes the form:

$$\rho = \frac{1}{4}[I_4 + r_{BB}^{opt}\boldsymbol{n}_B \cdot \boldsymbol{\sigma} \otimes \boldsymbol{n}_B \cdot \boldsymbol{\sigma} + r_{\theta\theta}^{opt}\boldsymbol{n}_\theta \cdot \boldsymbol{\sigma} \otimes \boldsymbol{n}_\theta \cdot \boldsymbol{\sigma} + r_{\phi\phi}^{opt}\boldsymbol{n}_\phi \cdot \boldsymbol{\sigma} \otimes \boldsymbol{n}_\phi \cdot \boldsymbol{\sigma}], \tag{S42}$$

indicating that this bound is unachievable without the introduction of an ancillary system. From the error propagation formula in Eq.(S20), we set $w_B = 1, w_\theta = B^2, w_\phi = B^2 \sin^2\theta$, then the precision limits of estimating three components of a vector field is

$$\delta B_{x_{\text{est}}}^2 + \delta B_{y_{\text{est}}}^2 + \delta B_{z_{\text{est}}}^2 \geq \frac{1}{32}\left(\frac{1}{T} + \frac{2B}{|\sin(BT)|}\right)^2. \tag{S43}$$

Without loss of generality, we set $\vec{B}_1 = \vec{B}_2 = \vec{B}$, the precision limit for estimating gradients $\nabla\vec{B} = \vec{B}_1 - \vec{B}_2 = (\nabla B_x, \nabla B_y, \nabla B_z)$ is

$$\delta\nabla B_{x_{\text{est}}}^2 + \delta\nabla B_{y_{\text{est}}}^2 + \delta\nabla B_{z_{\text{est}}}^2 \geq \frac{1}{16}\left(\frac{1}{T} + \frac{2B}{|\sin(BT)|}\right)^2. \tag{S44}$$

It is important to note that achieving the ultimate precision as outlined in Eq.(S44) requires the use of an ancillary system, making this bound unattainable in practice. To ensure a fair comparison, we introduce a reference precision using maximally entangled states, represented by the probe state $|\psi\rangle = \frac{1}{\sqrt{2}}(|00\rangle + |11\rangle)$. The QFIM for estimating $\hat{x} = \{B, \theta, \phi\}$ by maximally entangled states is

$$F_Q = \begin{pmatrix} [F_Q]_{BB} & [F_Q]_{B\theta} & [F_Q]_{B\phi} \\ [F_Q]_{B\theta} & [F_Q]_{\theta\theta} & [F_Q]_{\theta\phi} \\ [F_Q]_{B\phi} & [F_Q]_{\theta\phi} & [F_Q]_{\phi\phi} \end{pmatrix} \tag{S45}$$

with

$$\begin{aligned}
[F_Q]_{BB} =& 4T^2\left(3 + \cos(2\theta) + 2\cos(2\phi)\sin^2\theta\right), \\
[F_Q]_{\theta\theta} =& 2\sin^2(BT)\left(3 + 3\cos(2BT)\cos(2\phi) + 2\sin^2\phi + \cos^2(BT)\left(2 - 4\cos(2\theta)\sin^2\phi\right)\right. \\
&\left. + 4\cos\theta\sin(2BT)\sin(2\phi)\right), \\
[F_Q]_{\phi\phi} =& 2\sin^2(BT)\sin^2\theta\left(2 + 2\sin^2(BT) + 2\sin^2\theta + 2\sin^2\phi + \cos(2BT)\left(\cos(2\theta) - 3\cos(2\phi)\right)\right. \\
&\left. + 2\sin^2(BT)\cos(2\theta)\cos(2\phi) - 4\sin(2BT)\cos\theta\sin(2\phi)\right), \\
[F_Q]_{B\theta} =& 4T\left(2\sin^2(BT)\sin\theta\sin(2\phi) - \sin(2BT)\sin(2\theta)\sin^2\phi\right), \\
[F_Q]_{B\phi} =& -16T\sin(BT)\sin^2\theta\sin\phi\left(\cos(BT)\cos\phi + \sin(BT)\cos\theta\sin\phi\right), \\
[F_Q]_{\theta\phi} =& 2\sin^2(BT)\left(\sin(2BT)\sin\theta\left((3 + \cos 2\theta)\cos(2\phi) + 2\sin^2\theta\right) - 2\cos(2BT)\sin(2\theta)\sin(2\phi)\right),
\end{aligned} \tag{S46}$$

which is a singular matrix. This means we cannot simultaneously estimate three components of the vector fields. Instead, we consider the optimal precision of estimating three parameters respectively, expressed as $\delta x_{j_{\text{est}}}^2 \geq \frac{1}{[F_Q]_{x_j x_j}}$ for $x_j \in \{B, \theta, \phi\}$, then we have the total precision for estimating three components of a vector field as

$$\begin{aligned}
\delta B_{x_{\text{est}}}^2 + \delta B_{y_{\text{est}}}^2 + \delta B_{z_{\text{est}}}^2 &= \delta B_{\text{est}}^2 + B^2\delta\theta_{\text{est}}^2 + B^2\sin^2\theta\delta\phi_{\text{est}}^2 \\
&\geq \frac{1}{[F_Q]_{BB}} + \frac{B^2}{[F_Q]_{\theta\theta}} + \frac{B^2\sin^2\theta}{[F_Q]_{\phi\phi}}.
\end{aligned} \tag{S47}$$

Thereby the corresponding precision for estimating the gradients is

$$\delta\nabla B_{x_{\rm est}}^2 + \delta\nabla B_{\rm yest}^2 + \delta\nabla B_{z_{\rm est}}^2 \geq \frac{2}{[F_Q]_{BB}} + \frac{2B^2}{[F_Q]_{\theta\theta}} + \frac{2B^2\sin^2\theta}{[F_Q]_{\phi\phi}}. \tag{S48}$$

However, this precision is unachievable, which is a reference precision that equals the summation of the optimal precision for single-parameter estimation.

Now we turn the focus on estimating two components of gradients, $\hat{x} = (\nabla B_x, \nabla B_y)$. By a similar analysis as Eq.(S37), we have

$$\begin{aligned} w_B\delta B_{j_{\rm est}}^2 + w_\phi\delta\phi_{j_{\rm est}}^2 \geq & \frac{1}{4}\left(\frac{w_B}{\langle\Delta^2 G_B\rangle} + \frac{w_\phi}{\langle\Delta^2 G_\phi\rangle}\right) \\ = & \frac{1}{4}\left(\frac{w_B/T^2}{2+2r_{BB}-\left(r_B^{(1)}+r_B^{(2)}\right)^2} + \frac{w_\phi/\sin^2(BT)}{2+2r_{\phi\phi}-\left(r_\phi^{(1)}+r_\phi^{(2)}\right)^2}\right) \\ \geq & \frac{1}{4}\left(\frac{w_B/T^2}{2+2r_{BB}} + \frac{w_\phi/\sin^2(BT)}{2+2r_{\phi\phi}}\right) \\ \geq^{a)} & \frac{1}{4}\left(\frac{w_B}{4T^2} + \frac{w_\phi}{4\sin^2(BT)}\right) \end{aligned} \tag{S49}$$

The inequality $a)$ is obtained by using the properties in Eq.(S39), which gives $r_{BB} \leq 1$ and $r_{\phi\phi} \leq 1$. Moreover, $r_{\theta\theta} \geq -1$ and by subtitude $r_{BB} = r_{\phi\phi} = 1$ into constraints in Eq.(S39) gives the condition $r_{\theta\theta} \leq -1$. Hence, the inequality $b)$ is saturated when

$$r_{BB}^{opt} = 1, \quad r_{\theta\theta}^{opt} = -1, \quad r_{\phi\phi}^{opt} = 1, \tag{S50}$$

and $r_B^{(1)} + r_B^{(2)} = r_\phi^{(1)} + r_\phi^{(2)} = 0$. The corresponding optimal probe state is

$$\rho = \frac{1}{4}[I_4 + \boldsymbol{n}_B\cdot\boldsymbol{\sigma}\otimes\boldsymbol{n}_B\cdot\boldsymbol{\sigma} - \boldsymbol{n}_\theta\cdot\boldsymbol{\sigma}\otimes\boldsymbol{n}_\theta\cdot\boldsymbol{\sigma} + \boldsymbol{n}_\phi\cdot\boldsymbol{\sigma}\otimes\boldsymbol{n}_\phi\cdot\boldsymbol{\sigma}] = |\psi_{opt}\rangle\langle\psi_{opt}| \tag{S51}$$

Here $\theta = \frac{\pi}{2}$ and $|\psi_{opt}\rangle = \frac{1}{\sqrt{2}}\left(|+_B\rangle^{\otimes 2} - |-_B\rangle^{\otimes 2}\right)$, where $|\pm_B\rangle$ are the eigenstates of the generator h_B corresponding to the maximal and minimal eigenvalues respectively. With the optimal probe state, we can obtain the maximal QFIM for estimating $\hat{x} = \{B, \phi\}$ as

$$F_Q^{max} = \begin{pmatrix} 16T^2 & 0 \\ 0 & 16\sin^2(BT) \end{pmatrix} \tag{S52}$$

Measurement in the Bell basis, as detailed in Eq.(S15), is the optimal measurement strategy that saturates the quantum Cramér-Rao bound. Hence, the bound in Eq.(S49) is achievable. By setting $w_B = 1$ and $w_\phi = B^2$, the corresponding precision of estimating two components of the vector field is

$$\delta B_{x_{\rm est}}^2 + \delta B_{y_{\rm est}}^2 = \delta B_{\rm est}^2 + B^2\delta\phi_{\rm est}^2 \geq \frac{1}{16T^2} + \frac{B^2}{16\sin^2(BT)}, \tag{S53}$$

thereby the ultimate precision for estimating the gradients under this strategy is

$$\delta\nabla B_{x_{\rm est}}^2 + \delta\nabla B_{y_{\rm est}}^2 \geq \frac{1}{8T^2} + \frac{B^2}{8\sin^2(BT)}. \tag{S54}$$

It is worth mentioning that the optimal probe state in Eq.(S51) depends on the unknown parameters B and ϕ. However, the values of these parameters generally are not known as a priory. Instead, we must rely on estimated values, denoted as B_{est} and ϕ_{est}, which need to be adaptively updated in practice.

For easier experiment implementation, here, we also provide the precision of estimating gradient by using the maximally entangled state $|\psi\rangle = \frac{1}{\sqrt{2}}(|00\rangle + |11\rangle)$. The QFIM for estimating $\hat{x} = \{B, \phi\}$ by using maximally entangled state is

$$F_Q = \begin{pmatrix} 16T^2\cos^2\phi & -4T\sin(2BT)\sin(2\phi) \\ -4T\sin(2BT)\sin(2\phi) & 7 - 8\cos(2BT) + 2\cos(4BT)\cos^2\phi - \cos(2\phi) \end{pmatrix} \tag{S55}$$

The quantum Cramér-Rao bound can be saturated by using the projective measurement in Bell basis, as described in Eq.(S15). Hence, we have

$$\begin{aligned} \delta B^2_{\text{est}} &= [\text{Cov}(\hat{x})]_{11} \geq [F_Q^{-1}]_{11} = \frac{1 - \cos^2(BT)\cos^2\phi}{16T^2\sin^2(BT)\cos^2\phi}, \\ \delta\phi^2_{\text{est}} &= [\text{Cov}(\hat{x})]_{22} \geq [F_Q^{-1}]_{22} = \frac{1}{16\sin^4(BT)} \end{aligned} \tag{S56}$$

Then the precision of estimating two components of the vector field by maximally entangled states is

$$\begin{aligned} \delta B^2_{x_{\text{est}}} + \delta B^2_{y_{\text{est}}} = \delta B^2_{\text{est}} + B^2\delta\phi^2_{\text{est}} &\geq \frac{1}{16\sin^2(BT)}\left(\frac{1 - \cos^2(BT)\cos^2\phi}{T^2\cos^2\phi} + \frac{B^2}{\sin^2(BT)}\right) \\ &= \frac{1}{16\sin^2(BT)}\left(\frac{B^2 - \cos^2(BT)B_x^2}{T^2B_x^2} + \frac{B^2}{\sin^2(BT)}\right). \end{aligned} \tag{S57}$$

Similarly, the precision for estimating the gradients by maximally entangled states is

$$\delta\nabla B^2_{x_{\text{est}}} + \delta\nabla B^2_{y_{\text{est}}} \geq \frac{1}{8\sin^2(BT)}\left(\frac{B^2 - \cos^2(BT)B_x^2}{T^2B_x^2} + \frac{B^2}{\sin^2(BT)}\right). \tag{S58}$$

3. *Strategy comparison*

In addition to the two gradient-sensing approaches discussed above—direct gradient estimation using non-local entanglement (NLE) and a two-step approach that first estimates each vector field with local entanglement (LE) separately before calculating the gradient—we also consider an alternative approach based on the remote sensing (RS) described in the first section. In this approach, the remote magnetic fields at each location are estimated independently, with the central module serving as an ancilla, and the gradient is calculated from the separate field estimates. For a more comprehensive comparison, we also present the precision of gradient estimation achievable with this alternative strategy. The comparison is made under the condition that the resource allocation is identical, with each sensor module containing two sensors. In the following tables, we list the precision achieved by various strategies for estimating gradients in two and three directions, respectively.

In the main text, we have provided a detailed theoretical and experimental comparison of various strategies for estimating a two-component gradient. For completeness, Figure S1 gives the

Strategy	Initial state	Precision	Optimality	Achievability
NLE	$\frac{1}{\sqrt{2}}(\|0011\rangle - \|1100\rangle)$	$\frac{4B^2-3B_z^2}{16B^2T^2} + \frac{5B^2+3B_z^2}{16\sin^2(BT)}$	N	Y
RS	$\frac{1}{\sqrt{2}}(\|00\rangle + \|11\rangle)$	$\frac{1}{4T^2} + \frac{B^2}{2\sin^2(BT)}$	Y	Y
LE	N.A.	$\frac{1}{16}\left(\frac{1}{T} + \frac{2B}{\|\sin(BT)\|}\right)^2$	Y	N
	$\frac{1}{\sqrt{2}}(\|00\rangle + \|11\rangle)$	$\frac{2}{[F_Q]_{BB}} + \frac{2B^2}{[F_Q]_{\theta\theta}} + \frac{2B^2\sin^2\theta}{[F_Q]_{\phi\phi}}$	N	N

Table S1. The precision for estimating gradients along x, y and z directions.

Strategy	Initial state	Precision	Optimality	Achievability
NLE	$\frac{1}{\sqrt{2}}(\|0011\rangle - \|1100\rangle)$	$\frac{1}{4T^2} + \frac{B^2}{4\left(1+3\sin^2(BT)\right)\sin^2(BT)}$	N	Y
RS	$\frac{1}{\sqrt{2}}(\|00\rangle + \|11\rangle)$	$\frac{1}{4T^2} + \frac{B^2}{4\sin^2(BT)}$	Y	Y
LE	$\frac{1}{\sqrt{2}}\left(\|+_B\rangle^{\otimes 2} - \|-_B\rangle^{\otimes 2}\right)$	$\frac{1}{8T^2} + \frac{B^2}{8\sin^2(BT)}$	Y	Y
	$\frac{1}{\sqrt{2}}(\|00\rangle + \|11\rangle)$	$\frac{1}{8\sin^2(BT)}\left(\frac{B^2-\cos^2(BT)B_x^2}{T^2B_x^2} + \frac{B^2}{\sin^2(BT)}\right)$	N	Y

Table S2. The precision for estimating gradients along x and y directions.

comparison of strategies for estimating a three-component gradient. To ensure a fair comparison, we include the precision limit of Strategy LE utilizing maximally entangled states. Although employing the theoretically unachievable lower bound of Strategy LE, as derived in Eq.(S44), may not seem fair, it still highlights the enhanced precision of Strategy NLE across certain parameter value ranges. For example, at $B = 1$ and $\theta = \pi/2$, Strategy NLE demonstrates higher precision than Strategy LE during short encoding times T. Notably, despite the initial state of Strategy NLE not being optimal, and hence not achieving the highest possible precision, it still surpasses the best precision achievable by strategies without non-local entanglement. This emphasizes the significant advantages of distributed quantum sensing, demonstrating its superiority in achieving enhanced precision.

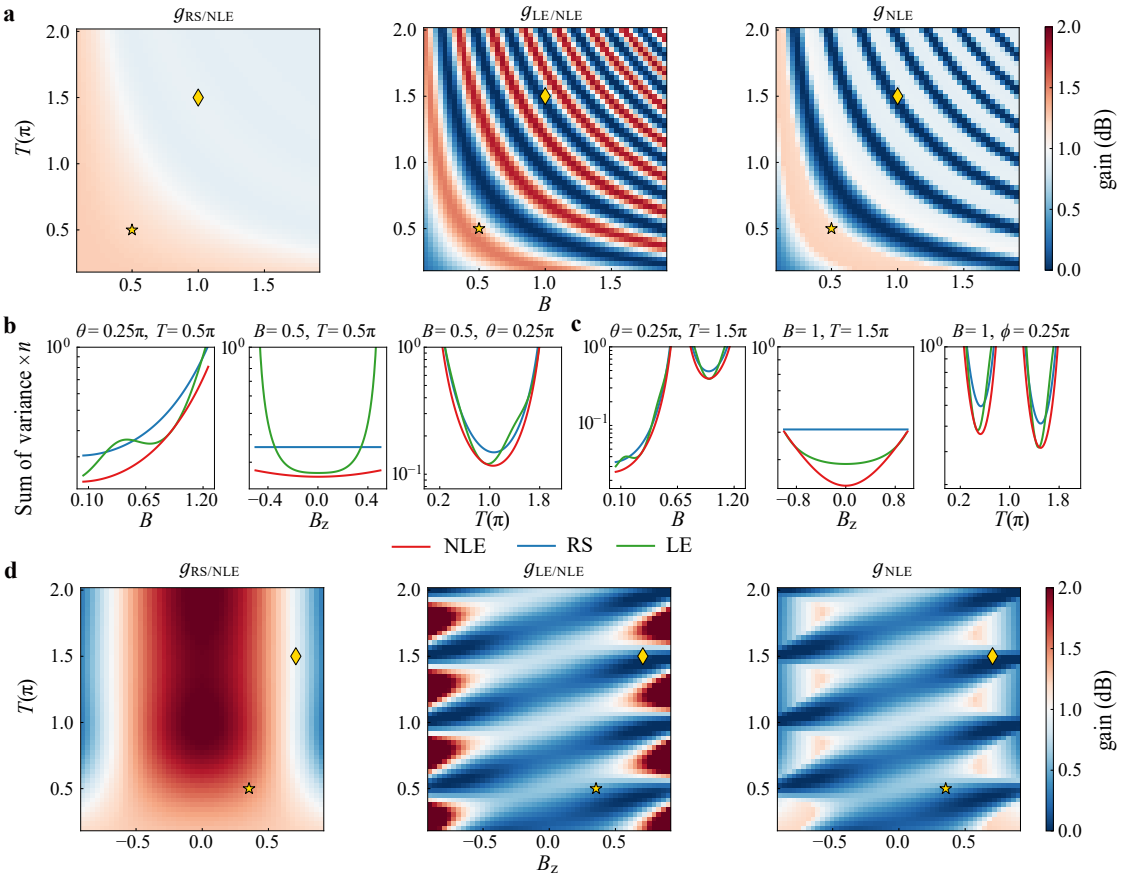

Fig. S1. **Comparing different strategies for estimating a 3-component gradient.** The x-component and y-component of the gradient are set of equivalent proportions. The stars mark the parameter set: $B = 0.5,\ T = 0.5\pi$; the diamonds mark the parameter set: $B = 1,\ T = 1.5\pi$. **a,** The advantage of NLE at $\theta = \pi/4$ when B and T are varying. **b,** The precision limits of three strategies around $B = 0.5,\ T = 0.5\pi$. Left: θ and T are fixed, B is varying from 0.05 to 1.25. Middle: B and T are fixed, B_z is varying from -0.5 to 0.5. Right: B and θ are fixed, T is varying from 0.1π to 1.9π. **c,** The precision limits of three strategies around $B = 1,\ T = 1.5\pi$. Left: θ and T are fixed, B is varying from 0.05 to 1.25. Middle: B and T are fixed, B_z is varying from -0.9 to 0.9. Right: B and θ are fixed, T is varying from 0.1π to 1.9π. **d,** The advantage of NLE at $B = 1$ when B_z and T are varying. In **a** and **d**, the left panels exhibit the gain of NLE over RS; the middle panels exhibit the gain of NLE over LE; the right panels exhibit the product of the gain of NLE over RS and the gain of NLE over LE.

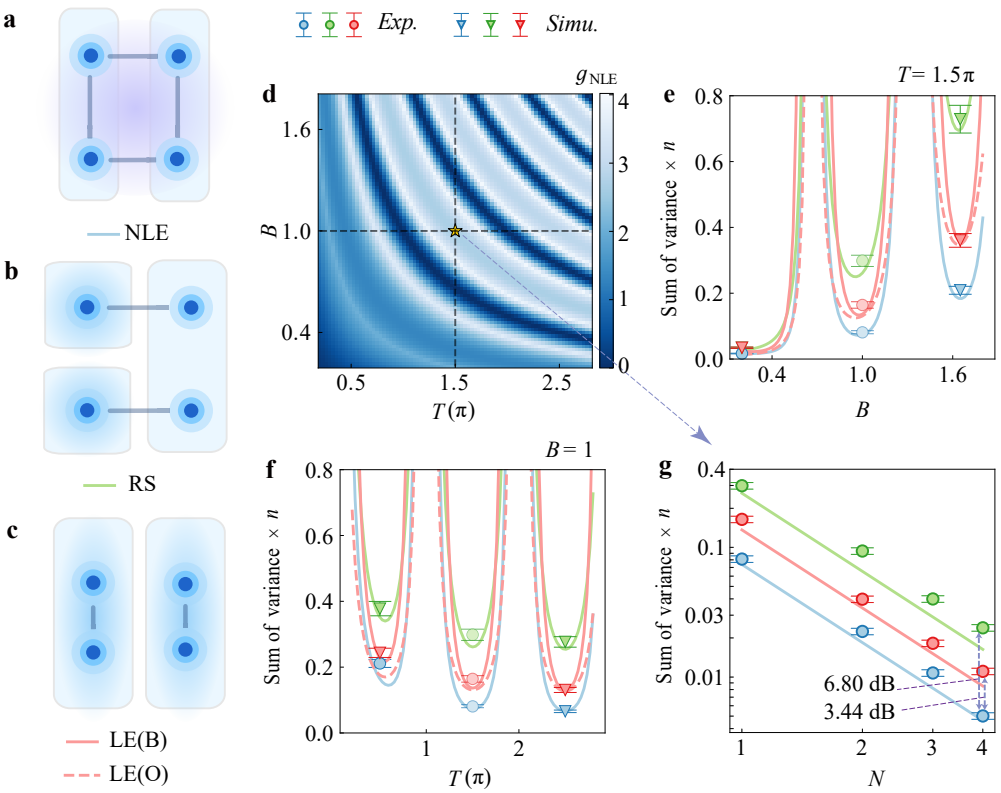

Fig. S2. **Strategies comparison for gradient estimation of a 2-component vector field. a-c,** Schematic diagrams of different strategies: (**a**) Distributed sensing with non-local entanglement (NLE); (**b**) Remote sensing (RS) with an ancilla qubit; (**c**) Sensing with local entanglement (LE). **d,** Parameter range where NLE outperforms RS and LE. The minimum precision gain of NLE over RS and LE(B) across different B and T values, is calculated by their theoretical precision. **e-f,** Comparison of the precision $(\sum_{i\in\{x,y\}} \delta^2 \nabla B_{i_{\mathrm{est}}})$ of the three strategies. (**e**) Precision versus B for the three strategies at $T = 1.5\pi$ and $N = 1$. (**f**) Impact of T on estimation precision at $B = 1$ and $N = 1$. (**g**) Estimation precision versus N for the three strategies at $T = 1.5\pi$ and $B = 1$. The solid and dashed curves: the theoretical precision bound. LE(B): local entanglement strategy using Bell state as the probe state, and Bell measurement. LE(O): local entanglement strategy using the optimal probe state and measurement.

II. EXPERIMENTAL IMPLEMENTATION

A. Device information

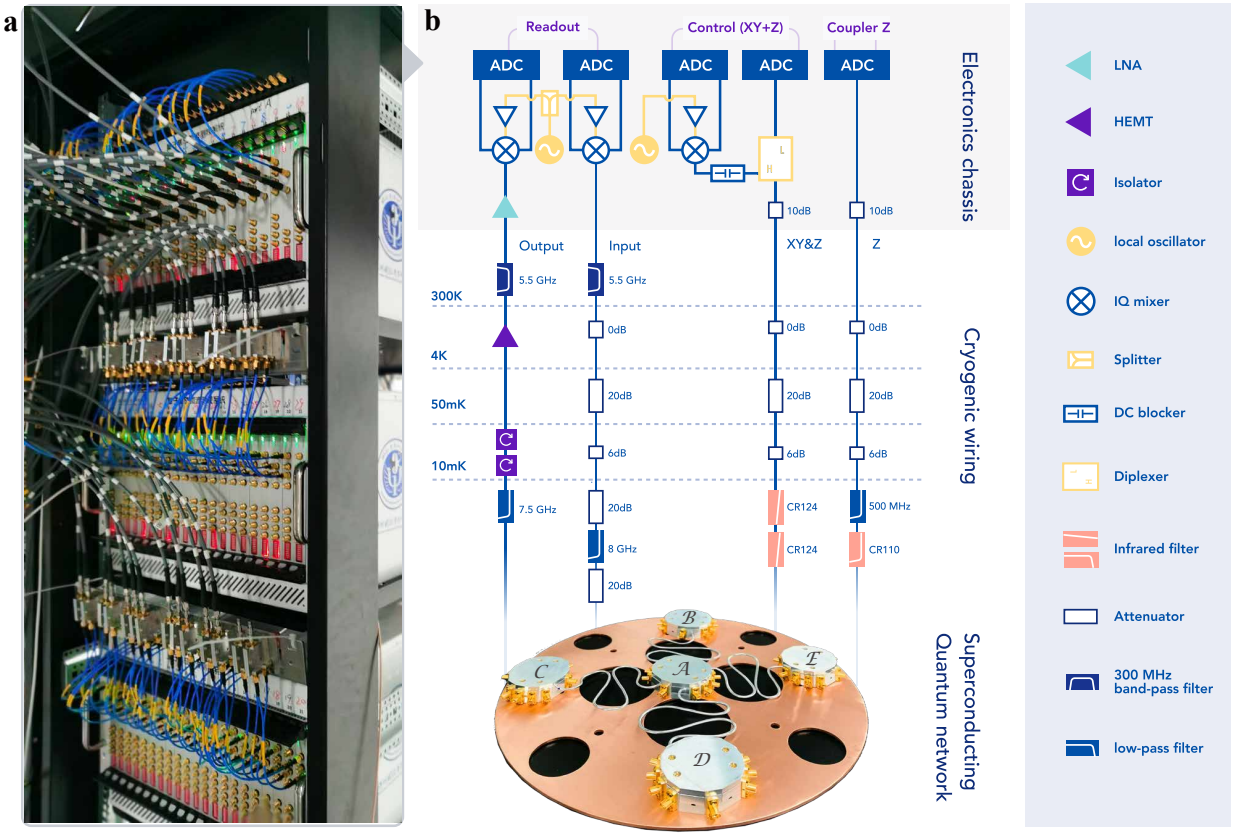

Fig. S3. **The experimental setup. a,** The microwave control and measurement system built for this experiment. **b,** The schematic diagram of the room-temperature electronics chassis, cryogenic wiring and superconducting quantum network inside of the dilution refrigerator. Right panel: the legend of the devices.

We implement the distributed quantum metrology experiment utilizing a modular quantum computing platform composed of five superconducting quantum chips, each integrated with four qubits. The inter-chip connectivity is facilitated by high-quality aluminum superconducting coaxial cables, where a gmon coupler is positioned between the qubits engaged in communication and the cable, enabling tunable coupling strength. Furthermore, an impedance transformer is designed on chip to significantly mitigate the stray loss on the communication channels [3]. In Fig. S3, we show the comprehensive structure of the experimental setup. The distributed quantum processors are sheltered in the 10 mK environment, nestled beneath the mixing chamber of a dilution refrigerator. The microwave cables connecting the superconducting quantum chips serve as the conduit for signal transmission and reception between the quantum processors (see the bottom part of the middle panel) and the customized integrated electronic channels (see the left photograph). The electron-

ics is primarily composed of digital-to-analog converters (DAC) and analog-to-digital converters (ADC), which orchestrate the generation, manipulation and readout of quantum control signals. The generation of XY control signals (single-qubit rotation) is facilitated by IQ mixing of the MHz output of the DACs and the GHz microwave carrier from a local oscillator (LO). Concurrently, the Z control signals (qubit frequency modulation) originate from DC and pulse signals output of the DACs. The XY signals and Z signals belonging to each qubit are combined with a customized diplexer in room temperature. The readout pulses are generated by another set of DACs, LO and IQ mixers, these devices up-convert the probe photons to match the readout resonator frequencies, conversely, the emitted photonic signals from the readout resonators are amplified and down-converted, finally being sampled by the ADCs, completing the readout cycle and providing a digital record of the measurement data. For higher control and readout quality, we deploy multiple filters across different temperature zones within the experimental setup (see the middle panel), the legends detailing the components of these stages are shown in the adjacent panel on the right.

Node	$\mathcal{A}$		$\mathcal{B}$		$\mathcal{C}$	
Qubit	Q_1	Q_2	Q_3	Q_4	Q_5	Q_6
$\omega_{\text{idle}}/2\pi$ (GHz)	4.551	5.019	4.477	4.959	4.937	4.393
$\omega_{\text{read}}/2\pi$ (GHz)	5.629	5.692	5.686	5.627	5.688	5.621
$E_C/2\pi$ (MHz)	-212	-200	-210	-225	-210	-229
F_{00}	0.94	0.94	0.88	0.86	0.92	0.90
F_{11}	0.91	0.90	0.87	0.83	0.88	0.89
T_1 (μs)	19.2	18.4	26.8	14.3	25.3	26.2
T_{2R} (μs)	1.52	4.77	2.42	4.72	3.58	4.02
T_{2E} (μs)	5.49	10.95	11.49	15.18	15.57	14.45
SQG RB fid(%)	99.96	99.91	99.95	99.47	99.80	99.75
CZ XEB fid(%)	98.50		97.30		98.40	

Table S3. Device information

The experiment in this work involves three distributed quantum processors, each containing two qubits. We list the basic information of these six qubits in Table S3. All qubits are designed to be operated across a frequency range of 4.1 $\sim$ 5.1 GHz, and idled at staggered frequencies. The resonator frequencies are also staggered for independent readout. The anharmonicity E_C is a parameter determined by the capacitance of each qubit, it is instrumental in shaping the interaction essential for the construction of CZ gates. F_{00} and F_{11} are the state preparation and measurement (SPAM) fidelity for $|0\rangle$ and $|1\rangle$. T_1 parameter denotes the energy relaxation time of each qubit, T_{2R} and T_{2E} represent the dephasing time characterized by Ramsey experiment and spin echo experiment, respectively.

B. Gate performance

We calibrate the CZ gates with a standard protocol[4]. We obtain CZ gate pulse with 36 ns plateau and 10 ns flattop rising and falling edges, and this gate is benchmarked using cross-entropy benchmarking (XEB) experiment [5], the fidelity turns out to be 98.1% in average.

The state transfer operation is calibrated by vacuum Rabi experiments between the inter-chip cable and the communication qubit to synchronize the frequencies of two qubits connecting on either side of the cable, aligning them to resonance. Concurrently, we tune the pulses applied on the tunable couplers to achieve an optimal coupling strength, reaching a low reflection loss[3]. The averaged transferred state fidelity measured by quantum state tomography is $\sim 98.4\%$.

The control-signal sequence is implemented by gate sets in U(3) formalism: $U_3(\alpha, \beta, \lambda) = R_z(\beta)R_x(\pi/2)R_z(\alpha)R_x(-\pi/2)R_z(\lambda)$. The gate set consists of three Z gates with three independent angles (λ, α, β). These Z gates are interleaved with an $X/2$ gate and a $-X/2$ gate. The single qubit gates (SQG) are benchmarked by randomized benchmarking (RB) experiment, and we obtain an averaged fidelity: 99.81%.

C. Implementation of distributed sensing in quantum circuits

The NLE strategy for gradient metrology is realized as illustrated in Fig. S4. We construct a three-node sensor network comprising modules $\mathcal{A}$, $\mathcal{B}$, $\mathcal{C}$. Initially, We generate a Bell pair between Q_1 and Q_2 on module $\mathcal{A}$, then simultaneously transfer one qubit of this pair from Q_1 to Q_3 on module $\mathcal{B}$ and another from Q_2 to Q_5 on module $\mathcal{C}$. Immediately thereafter, we apply CNOT gates on both $\mathcal{B}$ and $\mathcal{C}$, and obtain the GHZ state across module $\mathcal{B}$ and $\mathcal{C}$, with a fidelity of 80.36% (see Fig. S4(c)). The probe state $|\Psi_0\rangle$ is prepared by applying additional X gates on Q_3 and Q_4, and a Z gate on Q_5, achieving a fidelity of 76.16% (see Fig. S4(d)). Subsequently, we encode the spatially distributed vector field on sensor chips $\mathcal{B}$ and $\mathcal{C}$ with $U(3)$-formalism gate sets, where $\vec{B}_1$ is acting on both Q_3 and Q_4, $\vec{B}_2$ is acting on both Q_5 and Q_6. Following the encoding process, we conduct Bell measurement on both modules $\mathcal{B}$ and $\mathcal{C}$. Under optimal control, the ideal final state $|\Psi_f\rangle$ has equivalent occupation on $|0010\rangle$ and $|1000\rangle$, the fidelity obtained from experiment is 75.20% (see Fig. S4(e)). The information carried on the sensors are decoded into the probability distribution in measurement basis (see Fig. S4(f) for P_{0010}). The oscillation period over gradient components ∇B_x and ∇B_y are observed to reduce with increasing sequential copies N.

The error in this sequence primarily stems from the control error when synchronously transferring two entangling states. The control error is estimated to be 11.44% for generating the non-local GHZ state, the decoherence error throughout this 340 ns sequence is approximately 8.34%, estimated by numerical simulation. These two parts yields an estimated fidelity of 80.22%, which is closed to our experimental result of 80.36%. The non-local entangling state across two chips, which are not directly connected, is more fragile to environmental noise. The effective decoherence

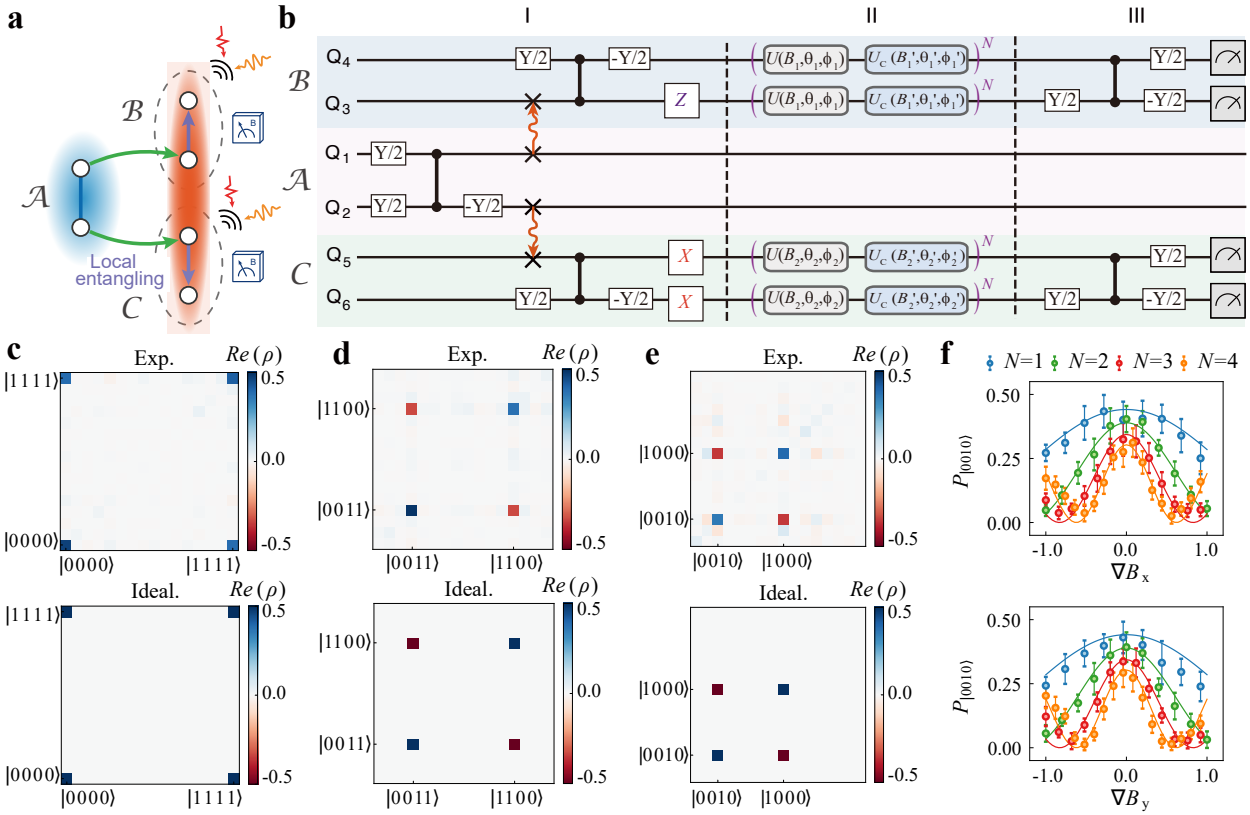

Fig. S4. **a,** A brief schematic diagram of NLE metrology strategy for gradient. **b,** The detailed quantum circuit of (a). **c,** The remote four-qubit GHZ state generated across three modules. **d,** The four-qubit probe state $|\Psi_0\rangle = \frac{1}{\sqrt{2}}(|0011\rangle - |1100\rangle)$. **e,** The reference final state $|\Psi_f\rangle = \frac{1}{\sqrt{2}}(|0010\rangle - |1000\rangle)$ after step III, with no control and signal units inserted into the circuit. **f,** The probability oscillation observed when scanning parameter ∇B_x or ∇B_y for different N, the encoding time is fixed at $T = 0.2\pi$.

rate of the probe state is estimated to be $80 \times 2\pi$ kHz by numerical analysis. As a consequence, the fidelity values of $|\Psi_f\rangle$ are $69.27\%, 63.81\%, 58.78\%, 54.15\%$ for $N = 1 \sim 4$, respectively. These values are higher than the confidence threshold $\sim 50\%$ for entanglement.

Demonstrating RS strategy requires two pairs of distributed nodes ($\mathcal{A}-\mathcal{B}$ and $\mathcal{A}-\mathcal{C}$) with high-quality connection. We take $\mathcal{A}$-$\mathcal{B}$ as an example (Fig. S5**a**), we transfer the local entanglement (indicated by the blue shadow) to a remote node, thereby establishing the cross-module entanglement (indicated by the red shadow). In our conception, the metrology of a local field through a sensor network comprising a central measurement module and multiple sensor modules spatially positioned for sensing. The quantum circuit is illustrated in Fig. S5(b). Initially, we generate a local Bell state on chip $\mathcal{A}$, and subsequently transfer this entangled state from Q_2 on chip $\mathcal{A}$ to Q_3 on module $\mathcal{B}$, resulting in a cross-node Bell state between Q_1 and Q_3. Immediately following the probe state preparation, we use Q_3 as the sensor qubit, Q_1 as the ancillary qubit. Assisted with dynamical decoupling sequence on Q_1 and Q_2, the inter-module entanglement is preserved from fast decoherence, until the quantum state on Q_3 is retrieved back to Q_2. The last step of this

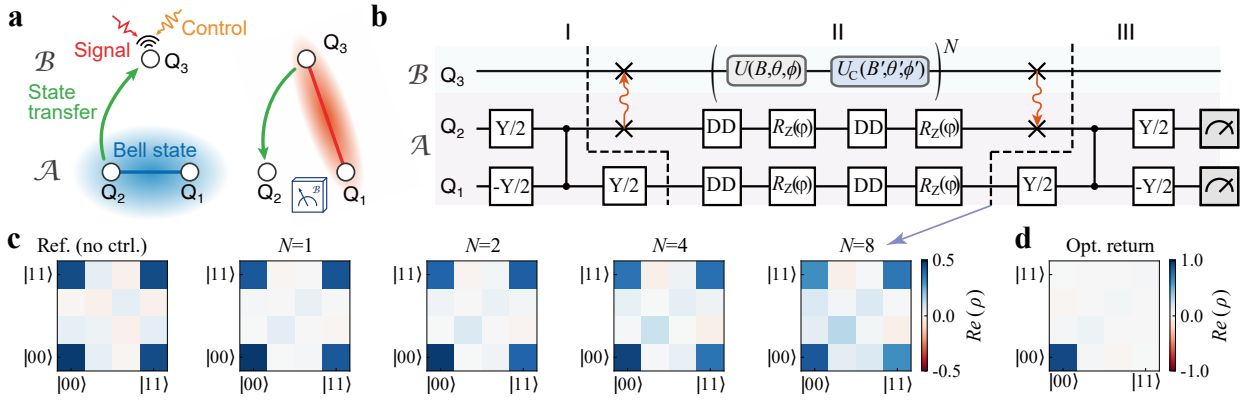

Fig. S5. **a,** A brief schematic diagram for sensing a local vector field at a certain position with two nodes $\mathcal{A}$ and $\mathcal{B}$. **b,** The quantum circuit diagram for **a**. I: state preparation, II: encoding, III: measurement. **c,** Ref (no ctrl): the density matrix with no signal-control sequence, measured after step II. $N = 1 \sim 4$: the density matrices with $N = 1, 2, 4, 8$, measured after step II. **d,** Opt return: the density matrix with no signal-control sequence, measured after step III.

process involves applying a Bell measurement on Q_1, Q_2. Under the optimal control conditions, step II behaves as an identity operator. We proceed to conduct quantum state tomography on module $\mathcal{A}$ after the encoded quantum state is retrieved. Fig. S5(c) shows the extracted real part of density matrices from Q_2 and Q_3.

The reference circuit, devoid of control and signal encoding in step II, achieves a final state fidelity of 91.15%. For $N = 1, 2, 4, 8$ in step II, we attain state fidelities of 88.13%, 84.37%, 79.02%, 70.46%, respectively. The reference final state is presented in the rightmost panel, the state fidelity is 90.52%. In this sequence, control error from the CNOT gates and state transfer operations amounts to 8.7%, the control error from each U_x or U_c unit is 0.79% in average, while the average decoherence error per unit is 2.55%, stemming from an effective decoherence rate of $41.1 \times 2\pi$ KHz.

A straightforward feature of the relation between control-signal layer N and the estimated precision can be captured by the oscillation period of probability under Bell measurement. As is shown in Fig. S6, the period of P_{00} profile near the optimal control parameters decreases at a rate proportional to N. Scanning each single parameter is analogous to a single-parameter-estimation process, wherein the quantum Fisher information is determined by the derivative of probability with respect to the parameter to be estimated. Therefore, this allows us to have an intuitive perception of the enhancement from sequential strategy. Moreover, the encoding time T is also periodically correlated to the probability distribution, and this correlation depends on the signal parameters. For example, when the signal is set to $(B, \theta, \phi) = (1, \pi/4, \pi/4)$, the period of P_{00} profile at $T = \pi, 2\pi$ stays invariant with respect to the parameters θ and ϕ, regardless of N. In contrast, at $T = 0.5\pi$ or $T = 1.5\pi$, the oscillation period changes more dramatically, indicating that the sequential strategy is effective there.

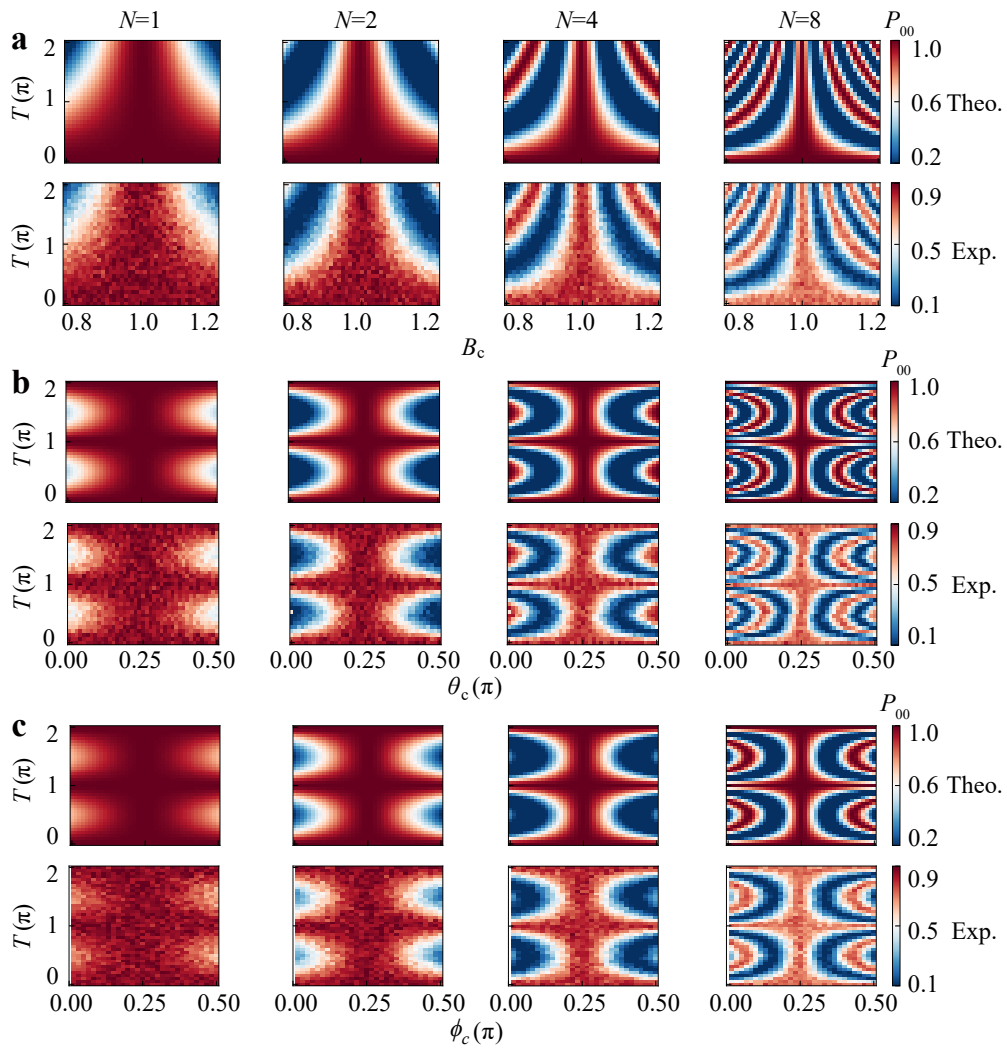

Fig. S6. **The probability oscillation with three parameters and encoding time T. a,** For a fixed signal, we scan control parameter B_c and encoding time T for different N. **b,** We scan control parameter θ_c and encoding time T for different N. **c,** We scan control parameter ϕ_c and encoding time T for different N.

To implement LE strategy, we generate local Bell state on node $\mathcal{B}$ and $\mathcal{C}$, signals and controls are simultaneously acting on two pairs of sensor qubits. The sequence ends with Bell measurement on $\mathcal{B}$ and $\mathcal{C}$, which is similar to RS strategy.

III. EXTENDED DATA

A. Extended data for sensing of remote vector fields

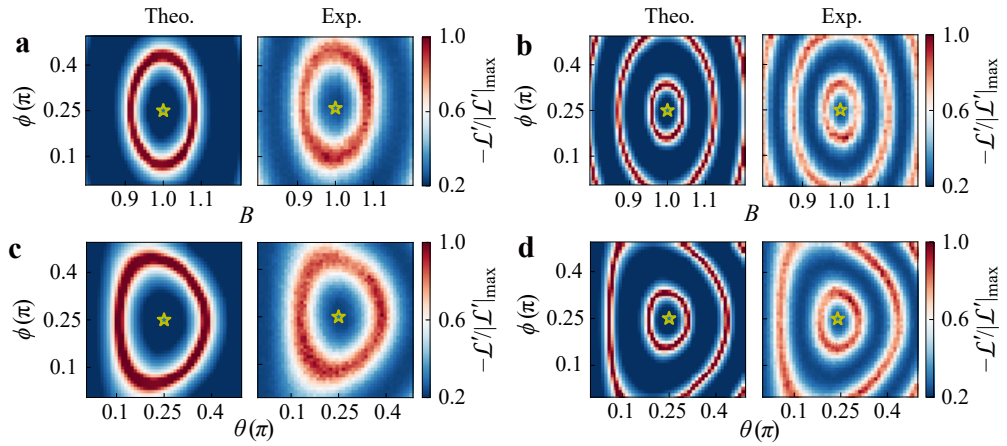

Fig. S7. **The likelihood function landscape at $N = 4$ and $N = 8$.** Stars: the location of the optimal control parameters. **a,** The landscape for parameter B and ϕ at $N = 4$. **b,** The landscape for parameter B and ϕ at $N = 8$. **c,** The landscape for parameter θ and ϕ at $N = 4$. **d,** The landscape for parameter θ and ϕ at $N = 8$. We post the theoretical landscape and experimental result, and mark the optimal control parameters.

We benchmark the sensor-ancilla network by analyzing the landscape of the likelihood function $\mathcal{L}'$ near the optimal control parameters, the results are shown over two variables in Fig. S7. Specifically, the panels depict $\mathcal{L}'(B, \phi)$ in Fig. S7**a,b** and $\mathcal{L}'(\theta, \phi)$ in Fig. S7**c,d**. The optimal control parameters, marked with a star in each panel, correspond to the expected estimation results. As N increases, the boundary area of the likelihood landscape contracts, demonstrated for $N = 4$ in Fig. S7**a,c** and $N = 8$ in Fig. S7**b,d**. The agreement between theoretical and experimental results ensures that the estimated parameters not only align with the observed data but also adhere to the underlying physical model.

The Fig. S8 illustrates the complete MLE result for sensing the three-component vector field. The density amplitude in each panel represents the count of distribution normalized by the integral of distribution at $N = 1$. These results demonstrate that increasing the number of sequential copies enhances the precision of simultaneous three-parameter estimation. However, unavoidable experimental errors introduce a bias of up to $\pm 3.45\%$ in the averaged estimation results, deviating from the actual vector field parameters. These errors can distort the likelihood landscape, affecting the efficiency of the MLE process. Moreover, fluctuation in experimental noise lead to inhomogeneous probability distributions, increasing the risk of convergence to local rather than global minima. Despite these challenges, the optimal strategy we implement facilitates a flat region around the optimal control parameters, and the use of multiple initial values mitigates the impact of local minima [6]. This approach improves the robustness and reliability of the estimation process [7].

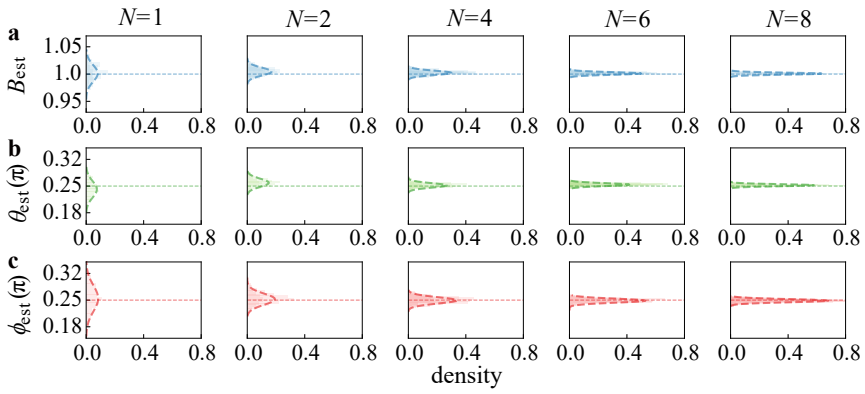

Fig. S8. **The result for simultaneously estimating three parameters of a local vector field $\vec{B}(B,\theta,\phi)$.** Bars: MLE result histograms. Dashed curves: gaussian fitting of the histograms. Dashed lines: the ideal signal parameters. **a,** The density distribution of parameter B. **b,** The density distribution of parameter θ. **c,** The density distribution of parameter ϕ.

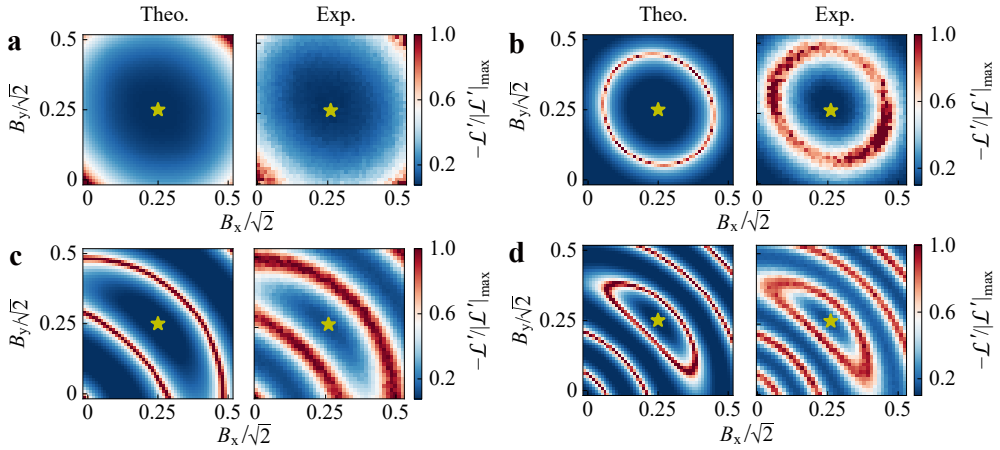

Fig. S9. **The theoretical and experimental landscape of estimating a two-component vector field with a sensor-ancilla network.** Stars: the location of the optimal control parameters. **a,** At $N = 2$ and $T = 0.5\pi$. **b,** At $N = 4$ and $T = 0.5\pi$. **c,** At $N = 2$ and $T = 1.5\pi$. **d,** At $N = 4$ and $T = 1.5\pi$

We apply the same benchmarking approach to a two-component vector field. As is shown in Fig. S9, the contraction of the likelihood function landscape with increasing N is evident. The parameters to be estimated in this case are set as $\vec{B} = (\frac{\sqrt{2}}{2}, \frac{\sqrt{2}}{2}, 0)$, corresponding to $|\vec{B}| = 0.5$.

B. Extended data for distributed sensing of vector field gradient

We experimentally evaluate the performance of NLE strategy for simultaneously estimating the three components of the gradient. In this scheme, we set $\vec{B} = (\frac{1}{2}, \frac{1}{2}, \frac{\sqrt{2}}{2})$, the normalized distributions of the estimators $\nabla B_{x_{\text{est}}}$, $\nabla B_{y_{\text{est}}}$, and $\nabla B_{z_{\text{est}}}$ are shown in Fig. S10**a** (for $T = 0.5\pi$) and Fig. S10**b** (for $T = 1.5\pi$).

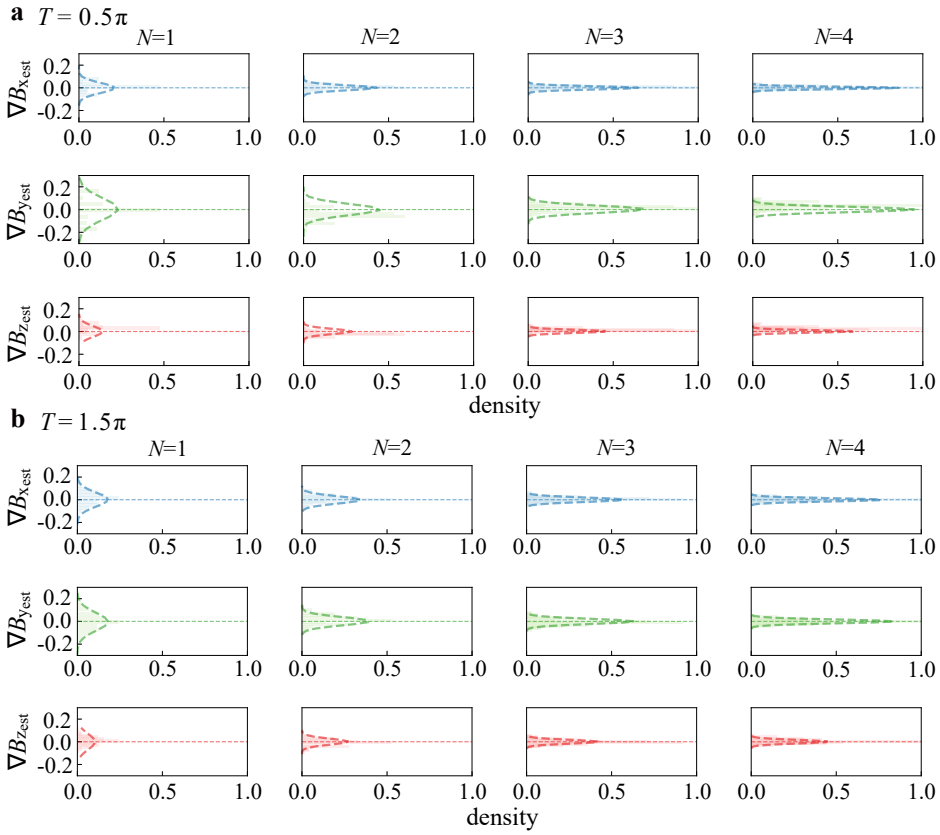

Fig. S10. **The normalized distribution of estimators for simultaneously three-component estimation.** Bars: MLE result histograms. Dashed curves: gaussian fitting of the histograms. Dashed lines: the ideal signal parameters. **a,** At $T = 0.5\pi$ and $N = 1 \sim 4$. **b,** At $T = 1.5\pi$ and $N = 1 \sim 4$.

When estimating the gradient of a two-component vector field $\nabla\vec{B} = (\nabla B_x, \nabla B_y)$, the field amplitudes are expressed as a function of gradient $\nabla\vec{B}$ and sum $\sum\vec{B}$ at two distinct positions, with $\vec{B}_1 = (\sum\vec{B} + \nabla\vec{B})/2$ and $\vec{B}_2 = (\sum\vec{B} - \nabla\vec{B})/2$. The full dataset, presented in Fig. 2 of the main text, is shown in Fig. S11, where the x and y components are plotted separately. The signal parameters are chosen as $\sum\vec{B} = (\sqrt{2}/2, \sqrt{2}/2, 0)$ and $\nabla\vec{B} = (0, 0, 0)$. The encoding times are set to $T = 0.5\pi$ (Fig. S11**a**) and $T = 1.5\pi$ (Fig. S11**b**).

C. The influence of noise

Different types of noise in quantum system have impact to the precision of the gradiometer. The effects of noisy channels in quantum parameter estimation have been discussed in previous studies [8–13]. In our work, the dominant sources of noise are control errors and dephasing. We numerically simulate the relationship between these noise types and the precision of the estimation. Fig. S12**a** shows the sum of variance in the estimated gradient as a function of different dephasing rates Γ_ϕ, while Fig. S12**b** depicts the effect of varying gate errors ϵ_σ on the precision. The dephasing noise is modeled using a thermal channel, and gate errors are incorporated through a Pauli noise

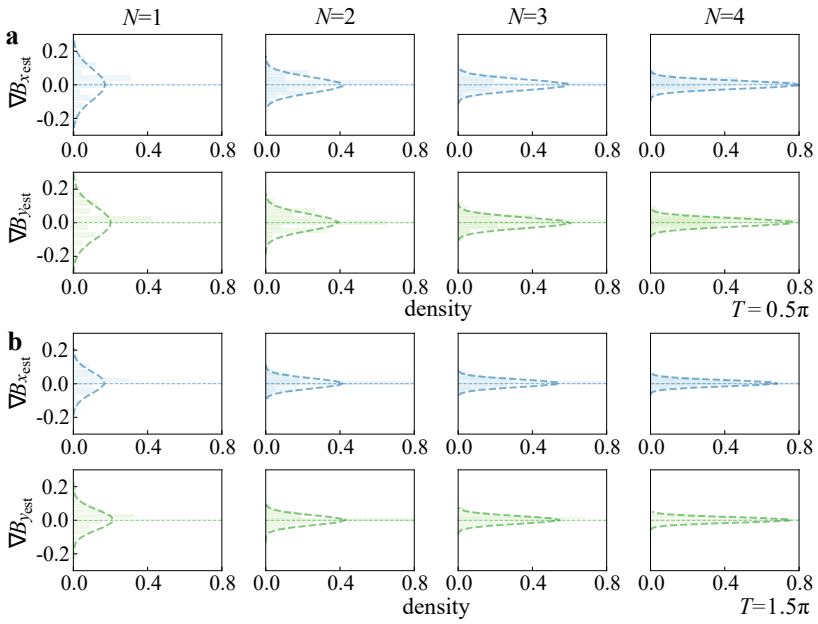

Fig. S11. **The density distribution for estimated x and y components of the vector field gradient.** Bars: MLE result histograms. Dashed curves: gaussian fitting of the histograms. Dashed lines: the ideal signal parameters. **a,** The density at $T = 0.5\pi$ for $N = 1, 2, 3, 4$. **b,** The density at $T = 1.5\pi$ for $N = 1, 2, 3, 4$.

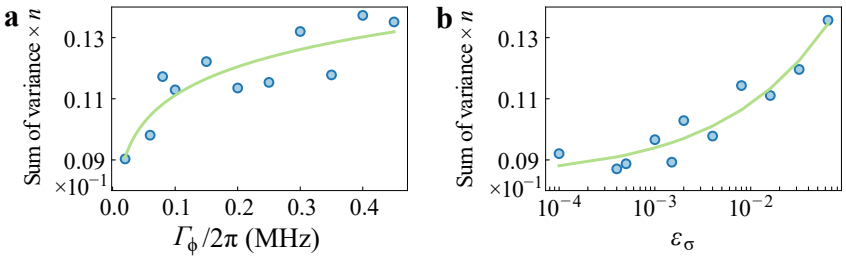

Fig. S12. **The influence of circuit error on the MLE result.** Dots: simulation data. Solid curves: fitting result. **a** The relation between simulated precision and dephasing rate. **b** The relation between simulated precision and gate error.

channel. These simulations are conducted using the Qiskit framework [14].

To mitigate the effects of noise, we apply error mitigation (EM) techniques [15] during data post-processing. For the NLE strategy, non-local entangled states are particularly sensitive to environmental noise. However, EM significantly improves performance, as demonstrated in Fig. S13.

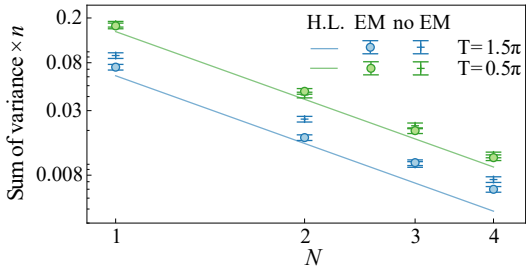

Fig. S13. **The effect of error mitigation (EM) on the experimental sum of variance.**

[1] Yuan, H. Sequential feedback scheme outperforms the parallel scheme for hamiltonian parameter estimation. *Phys. Rev. Lett.* **117**, 160801 (2016).

[2] Hou, Z. *et al.* Minimal tradeoff and ultimate precision limit of multiparameter quantum magnetometry under the parallel scheme. *Phys. Rev. Lett.* **125**, 020501 (2020).

[3] Niu, J. *et al.* Low-loss interconnects for modular superconducting quantum processors. *Nat. Electron.* **6**, 235–241 (2023).

[4] Sung, Y. *et al.* Realization of high-fidelity cz and zz-free iswap gates with a tunable coupler. *Phys. Rev. X* **11**, 021058 (2021).

[5] Goss, N. *et al.* High-fidelity qutrit entangling gates for superconducting circuits. *Nat. Commun.* **13** (2022).

[6] Kuroda, M., Mori, Y. & Iizuka, M. *Initial Value Selection for the Alternating Least Squares Algorithm*, 227–239 (Springer Singapore, 2020).

[7] Hou, Z. *et al.* Zero–trade-off multiparameter quantum estimation via simultaneously saturating multiple heisenberg uncertainty relations. *Sci. Adv.* **7**, eabd2986 (2021).

[8] Le, T. K., Nguyen, H. Q. & Ho, L. B. Variational quantum metrology for multiparameter estimation under dephasing noise. *Sci. Rep.* **13** (2023).

[9] Yuan, H. & Fung, C.-H. F. Quantum parameter estimation with general dynamics. *npj Quantum Inf.* (2017).

[10] Escher, B. M., de Matos Filho, R. L. & Davidovich, L. General framework for estimating the ultimate precision limit in noisy quantum-enhanced metrology. *Nat. Phys.* **7**, 406–411 (2011).

[11] Wang, K. *et al.* Entanglement-enhanced quantum metrology in a noisy environment. *Phys. Rev. A* **97**, 042112 (2018).

[12] Chaves, R., Brask, J. B., Markiewicz, M., Kołodyński, J. & Acín, A. Noisy metrology beyond the standard quantum limit. *Phys. Rev. Lett.* **111**, 120401 (2013).

[13] Peng, J.-X., Zhu, B., Zhang, W. & Zhang, K. Enhanced quantum metrology with non-phase-covariant noise. *Phys. Rev. Lett.* **133**, 090801 (2024).

[14] Javadi-Abhari, A. *et al.* Quantum computing with qiskit (2024). arXiv:2405.08810.

[15] Conlon, L. O. *et al.* Approaching optimal entangling collective measurements on quantum computing platforms. *Nat. Phys.* **19**, 351–357 (2023).